On the Thermal Stability of Aryl Groups Chemisorbed on Graphite

Hans Van Gorp,[a‡] Peter Walke,[a‡] Joan Teyssandier,[a] Brandon E. Hirsch,[a] Hiroshi Uji-i,[ab] Kazukuni Tahara,[c] Yoshito Tobe,[de] Mark Van der Auweraer,[a] Steven De Feyter[a]*

[a] Department of Chemistry, Division of Molecular Imaging and Photonics, KU Leuven-University of Leuven, Celestijnenlaan 200F, B-3001 Leuven, Belgium.

[b] RIES, Hokkaido University, N20W10, Kita-Ward, Sapporo, Japan.

[c] Department of Applied Chemistry, School of Science and Technology, Meiji University, 1-1-1 Higashimita, Tama-ku, Kawasaki, Kanagawa, 214-8571, Japan.

[d] Division of Frontier Materials Science, Graduate School of Engineering Science, Osaka University, Toyonaka, Osaka 560-8531, Japan

[e] The Institute of Scientific and Industrial Research, Osaka University, Ibaraki, Osaka 567-0047, Japan

‡: contributed equally

Abstract

The covalent functionalization of carbon-based materials through aryldiazonium chemistry has emerged as a powerful tool for physicochemical property modification. However, the characterization techniques traditionally used to assess the stability of any modification, such as thermogravimetric analysis (TGA), do not allow covalent detachment to be discriminated from the loss of physisorbed material. Here, we present a general method to differentiate these two processes by combining scanning probe microscopy with Raman spectroscopy. Using covalently modified highly oriented pyrolytic graphite (HOPG), we show that the thermally induced covalent bond breaking between the aryl groups and the HOPG surface can be directly monitored through this combined approach. Moreover, temperature-dependent Raman spectroscopy allows the kinetics of this bond breaking to be studied. Desorption activation energies can thus be initially estimated for aryl groups bearing different substituents. Finally, we highlight that the pristine HOPG structure can be restored at a relatively low temperature, opening the way for reversible covalent modification. Our results alight on a general methodology for the full characterization of covalently modified carbon materials.

Introduction

The ubiquity of carbon materials across many areas of science and technology is predicated on the wide variety of structures and properties they display. Interest is particularly focused on the family of sp^2-hybridized carbon allotropes, initiated by the respective discoveries of fullerenes, carbon nanotubes and latterly graphene, that are different allotropes of the same basic building block.[1] Substantive investigations continue into the fundamental properties of these materials as well as their potential implementation in numerous applications. However, the presence of large

delocalized π-electron systems gives rise to very strong aggregation, and consequently they have traditionally suffered from limited solution processability in their native forms. Chemical functionalization initially arose as a subsequent strategy to improve solubility,[2–7] but has more recently been extended further towards property optimization for specific applications or integration within new hybrid materials. Examples include fullerene derivatives as electron acceptors in bulk-heterojunction organic solar cells,[8] chemically modified carbon nanotubes to mechanically reinforce polymers,[9] or graphene-based sensors.[10]

Such functionalization can involve both physisorption and chemisorption.[7,11–13] Since no new chemical bonds are formed, physisorption offers a better preservation of intrinsic properties.[7,12,] But due to the weak intermolecular interactions between the molecules and the surface, such systems are likely to lack robustness, which may limit stability against elevated temperatures and other environmental changes. On the other hand, chemisorption is expected to lead to more stable functionalization, but generates localized sp^2 to sp^3 rehybridization, and so also more strongly modifies the pristine systems. Although the introduction of these "defects" can be detrimental to certain electronic properties such as carrier mobility,[14] it can also be used beneficially, for example to increase conductivity by changing the position of the Fermi-energy.[15] Various methods are used for this covalent attachment, but the reduction of arenediazonium salts is one of the most efficient and versatile.[16,17] Typically based on the reductive decomposition of an arenediazonium salt to produce an aryl radical that subsequently attacks (or "grafts" to) the carbon surface to form a C-C bond, with the correct choice of molecule a high density of covalent modification can be achieved on the basal plane.[18,19] The method is also very mature, with a vast library of compounds described in literature,[20,21] and adaptable to different environments since the reaction can be initiated *via*

various processes: spontaneous reactions,[22] as well as the chemical,[23] electrochemical[20,24] or photochemical reduction of diazonium salts.[25]

Since the main reason to choose covalent modification over physisorption is the expected superior stability of the chemisorbed species, it is of critical importance to study the thermal behavior of these functionalized carbon derivatives. This would allow environmental operating windows for individual applications to be established, and necessitates not only investigating the stability of chemisorbed molecules on the surface, but also determining local and global structural changes resulting from the elevated temperatures. Given the versatility of covalent modification, such behavior may in turn be unique to a specific molecule-substrate combination. It is therefore also crucial to understand how this choice of molecule could generate differences in stability, as well as in coverage and other, more emergent properties. Finally, it could inform on the feasibility and generality of using annealing to restore the pristine carbon lattice, as has been previously alluded to,[26] thereby allowing covalent modification to act as a transient step in a multi-stage process. Temperature programmed desorption (TPD) monitored by thermogravimetric analysis (TGA),[4,27] along with a variant coupled to mass spectroscopy (TGA-MS),[28–30]has been the traditional method of choice for studying these phenomena. But TGA only gives the mass loss occurring after physical desorption of the film/material from the carbon surface, resulting in no distinction between desorption of the physisorbed or chemisorbed material, and therefore requiring the assumption that desorption and covalent bond breaking occur concomitantly. This is particularly problematic for diazonium derivatives given they can polymerize and form multilayers that may in turn inhibit the physical desorption.[31] Raman spectroscopy, on the other hand, can specifically monitor the chemisorption on a global scale, with the so-called D band associated with defects in the lattice,[19,26,28,32–35] but usually cannot directly probe physisorption. Like TGA, it is

also blind to secondary processes occurring on the surface. The importance of scanning probe microscopy (SPM) techniques in this context has recently been shown: while scanning tunneling microscopy (STM) only images the chemisorbed species, atomic force microscopy (AFM) visualizes both chemisorbed and physisorbed species absorbed on the surface.[18] Combining Raman and SPM hence appears to be a powerful strategy to observe the outcome of thermally desorbed compounds by offering both insights on the local structure and chemical information at a larger scale. In this way the breaking of the covalent bond may be deconvoluted from desorption of the physisorbed species.

In this contribution we examine the thermal desorption of four different aryl derivatives covalently attached on highly oriented pyrolytic graphite (HOPG) *via* the electrochemical reduction of diazonium salts. While AFM reveals that most of the molecular layer remains on the surface after annealing up to 200 °C, STM and Raman confirm cleavage of the covalent bonds between the aryl groups and HOPG starts at temperatures no higher than 160 °C. Covalent linkages are almost entirely lost by 200 °C in all cases. This indicates that aryl units start to detach before they completely desorb from the HOPG surface. Moreover, Raman spectroscopy offers a rapid and straightforward way to follow the kinetics of bond breaking, and to estimate its substituent-dependent activation energy. An important consequence is the restoration of pristine, sp^2-hybridised HOPG at relatively low temperatures, opening the door to reversible covalent modifications, as well as suggesting implications for thermal operating windows in future applications.

Methods

Material. 4-Nitrobenzene diazonium (4-NBD) tetrafluoroborate (97%, Sigma-Aldrich Co. LLC), 3,4,5-trimethylaniline (98%, AK Scientific, Inc.), 3,4,5-trimethoxyaniline (97%, Sigma-Aldrich Co. LLC), 3,5-bis-*tert*-butylaniline (98%, Tokyo Chemical Industry Co., LTD.), analytical grade hydrochloric acid (Sigma-Aldrich Co. LLC) and aqueous $NaNO_2$ (99.999%, 0.1 M, Sigma-Aldrich Co. LLC) are commercially available and were used as received. Graphite substrates consisted of HOPG (grade ZYB, Advanced Ceramics Inc.). Ultrapure water (Milli-Q, Millipore, 18.2 MΩ cm, total organic carbon <3 ppb) was used for the preparation of solutions and rinsing.

Sample preparation. The HOPG substrates were functionalized using aryl radicals (Figure 1a). In turn, these were electrochemically (EC) generated from the derivatives of arenediazonium cations in a similar manner as reported previously.[18] Such cations can be obtained commercially, like 4-NBD or they can be generated *in-situ* from their corresponding aniline precursor, as was used to generate the cations 3,4,5-trimethylbenzene diazonium (3,4,5-TMeD), 3,4,5-trimethoxybenzene diazonium (3,4,5-TMeOD), and 3,5-bis-*tert*-butylbenzene diazonium (3,5-TBD). In both cases a chloride counter ion is used, as the component was dissolved in 5.0 mL of a 50mM HCL solution to reach a concentration of 2.0 mM. For the aniline derivatives a supplementary 100 µL of a 0.1 M $NaNO_2$ solution was added to initiate the diazotization. In that case, the solution is stirred for 1 min prior to injection into a homebuilt three-electrode EC cell. The setup consists of (1) a 50.3 mm^2 graphite working electrode (HOPG), (2) a Pt wire counter electrode, and (3) a Ag/AgCl/NaCl (3.0 M) reference electrode. Highly reactive aryl radicals are formed close to the working electrode by a one election reduction using cyclic voltammetry. In this process a covalent bond is formed between the aryl radical and the HOPG surface. Each procedure includes ramping the potential through three consecutive cycles from +0.2 V to −0.4 V at a scan rate of 0.1 V/s (Figure S1). The voltage sweeps were performed using an Autolab

PGSTAT101 potentiostat (Metrohm Autolab BV). Substrates were subsequently rinsed (ca. 50 mL) with Milli-Q water and dried under argon.

Atomic Force Microscopy. Atomic force microscopy is used for evaluating the morphological characteristics of the modified HOPG substrates. Additionally, the AFM setup is used to subject the sample through a series of controlled stepwise heating cycles by using the incorporated environmental cell and heating stage. All experiments were performed using a Cypher ES (Asylum Research) microscope with imaging always conducted at 32 °C and with probes only installed following each completed heating step to avoid any possible tip contamination. Images were obtained in tapping mode at the air/solid interface with minimized forces using OMCL-AC160TS-R3 probes (Olympus Corporation) at a resonance frequency of ± 300 kHz (spring constant ±26 N/ m). Prior to each heating cycle the AFM chamber was purged for 30 min with N_2 gas (40 mL/ min) (N_2 Alphagaz 1, Air Liquide) and with the inert atmosphere being maintained until the sample cooled down again. Each sample was successively subjected to five 30 min heating procedures with a ramp rate of 1 °C/s until 160, 170, 180, 190 and 200 °C. Each completed cycle was accompanied by Raman spectroscopy analysis, as well as STM and AFM characterization to evaluate the resulting impact on the sample surface.

Scanning Tunneling Microscopy. STM measurements were performed at room temperature at the air/solid interface with a PicoSPM (Agilent) instrument operating in constant current mode using a mechanically cut Pt/Ir (80/20) tip. The data was analyzed with Scanning Probe Image Processor 6.3.5 (SPIP, Image Metrology ApS) software.

Raman spectroscopy and kinetic experiments. Raman measurements were performed with an OmegaScope^{TM} 1000 (Horiba, formerly AIST-NT) and 632.8 nm laser light from a He-Ne laser was focused onto the sample surface using an objective (MITUTOYO, BD Plan Apo 100x, N.A.

0.7). The optical density at the sample surface was about 800 kW/cm^2. For the kinetics measurements a longer working distance objective was used (MITUTOYO, M Plan Apo SL 50x, N.A. 0.42), for which the optical density was around 300 kW/cm^2. Raman scattering was collected with the same objective in each case and directed to a Raman spectrograph (Horiba JY, iHR-320) equipped with a cooled charge coupled device (CCD) camera operated at -100 °C (Andor technology, DU920P-BRDD) through a pinhole, a dichroic mirror (Chroma Technology Corporation, Z633RDC) and long pass filter (Chroma Technology Corporation, HQ645LP). For the room temperature and sequential heating experiments, multiple (~6) measurements were performed at different positions for each sample and temperature step, and the results averaged to determine the final values given in the main text.

For the kinetics measurements, a heating chamber (Linkam, THMS600) was used to heat the samples in an inert environment (argon) and temperatures were determined simply from the given values on the Linkam stage. Before each measurement, the chamber containing the sample was purged with argon gas for several minutes. The objective was positioned outside the chamber and light focused onto the sample through a glass optical window. The chamber was heated to a specified temperature (ramp rate 150 °C/min) that was subsequently maintained for the duration of the measurements. To remove changes incurred during the ramping time, all changes in I_D/I_G were taken relative to the first measurement performed after reaching the desired temperature. Spectra were recorded successively (with an acquisition time of 10 seconds) at a single position and there were no pauses between consecutive spectra. Measurements were terminated when no D-band could be detected within a single acquisition or after approximately 300 seconds, though typically only the first 100 seconds were considered due to difficulty in determining changes at longer times. The reduced S/N (due to the lower acquisition time) also led to a consequent

reduction in the detection limit of the D-band. Occasionally for some individual measurements at low temperatures (e.g. 130/140 °C for the 3,5-TBD system), changes within 100 seconds were not clear and so a longer acquisition time of ~300 seconds was used. Measurements were recorded at a temperature interval of 10 °C, and typically at least 3 measurements were recorded for each temperature step. Temperatures ranged from 210 °C to 160 °C for the 3,4,5-TMeOD-G system, 200 °C to 160 °C for 3,4,5-TMeD-G and 160 °C to 130 °C for 3,5-TBD-G. Analysis of the rate constant was made assuming first-order reaction kinetics. All Raman measurements were processed using IGOR Pro.

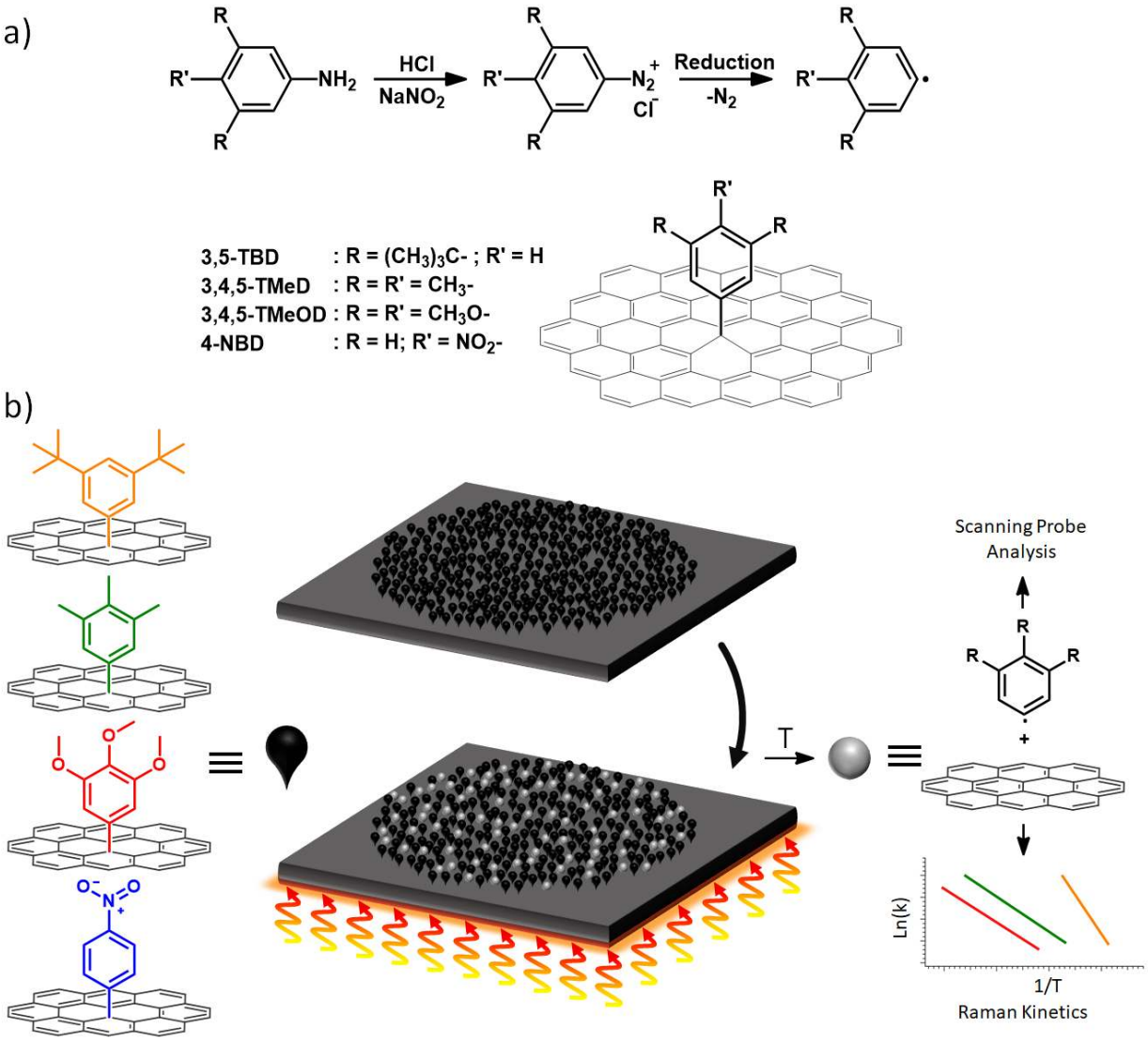

Figure 1. (a) Reaction scheme for the covalent functionalization of HOPG, showing the relevant substituent moieties for each of the molecules studied (3,5-TBD, 3,4,5-TMeD, 3,4,5-TMeOD and 4-NBD). (b) Temperature evolution. Covalently bound monolayers of each of the molecules in a) undergo a stepwise temperature treatment. At each stage, changes to the surface in terms of topography and loss of covalently bound species are investigated by Raman and SPM. Black pins represent the covalently bound species and grey dots the dissociated breakdown products. Finally, Raman measurements are used to investigate the kinetics of temperature-induced bond-breaking.

Results and Discussion

Room temperature investigation. HOPG samples were functionalized by four substituted arenediazonium salts, as shown in Figure 1a. These were respectively the cations 3,5-bis-*tert*-butyldiazonium (3,5-TBD), 3,4,5-trimethylbenzene diazonium (3,4,5-TMeD), 3,4,5-trimethoxybenzene diazonium (3,4,5-TMeOD) and 4-nitrobenzene diazonium. In some cases, the arenediazonium salts were generated directly *in situ* from the corresponding aniline derivative, though for clarity, we will hereafter refer to the diazonium form only. This led to the generation of 4 functionalized HOPG systems, hereafter referred to as 3,5-TBD-G, 3,4,5-TMeD-G, 3,4,5-TMeOD-G and 4-NBD-G. Further details on the functionalization procedure can be found in the methods section. Figure 1 outlines a generalized methodology for experiments (starting from the aniline derivative), with each of these systems subject to heating treatments and subsequently characterized by both Raman and SPM to determine their thermal evolution. Additional Raman measurements were also performed *in situ* to determine the kinetics of this thermal desorption.

The outcome of functionalization for each of the 4 systems was first investigated at room temperature, and this initial state following covalent modification is detailed in Figure 2. It is widely known that functionalization with 4-NBD yields a substantially reduced defect concentration in comparison to 3,5-TBD due to the formation of dendritic multilayers.[18] Furthermore, we recently reported a study into the dependency of graphitic functionalization on the nature of functional groups in the 3, 4 and 5 positions of electrochemically reduced trisubstituted, arenediazonium salts.[36] This included looking at 3,5-TBD, 3,4,5-TMeOD and 3,4,5-TMeD. Therein, it was found that 3,5-TBD-G and 3,4,5-TMeOD-G exhibited the greatest degree of functionalization, with the value being substantially lower in the case of 3,4,5-TMeD-G.

Moreover, a relation was observed between the degree of functionalization and the electron donating properties of the different functional groups for a series of aryldiazonium derivatives grafted on HOPG. This was explained partly by energy level matching between singly occupied molecular orbital (SOMO) levels of the aryl radicals and the Fermi level of the surface. However, given the differing experimental apparatus and experimental conditions, to confirm the generality of the reported findings, and to provide a basis for the subsequent measurements, it is also necessary to perform such measurements here.

Differences in the degree of covalent modification between the systems was first highlighted by Raman spectroscopy. Figure 2a shows typical Raman spectra for each of the functionalized HOPG systems at room temperature, focused on the 1200-1800 cm^{-1} spectral region. In principle, Raman spectroscopy quantifies the number of surface defects in the HOPG lattice through the ratio of the D (~1350 cm^{-1}) and G (~1580 cm^{-1}) bands, I_D/I_G ,[37–39] with higher values corresponding to a greater degree of covalent modification. This is discussed in greater detail below in the context of the kinetics measurements. It is known that I_D/I_G tends to saturate on HOPG somewhat above 0.1,[18] and in the present case, relevant I_D/I_G values are respectively 0.088 ± 0.002 for 3,5-TBD-G and 0.073 ± 0.003 for 3,4,5-TMeOD-G functionalized HOPG. Conversely, while the value for 3,4,5-TMeD-G sample was smaller at 0.037 ± 0.004, for the 4-NBD-G sample it was only 0.006 ± 0.002. From these values it can be deduced that 3,5-TBD-G and 3,4,5-TMeOD-G generated the greatest amount of covalent modification, while 4-NBD-G led to the least, and with 3,4,5-TMeD-G being somewhat intermediate.

To take advantage of the complementarity between techniques, corresponding STM analysis for each of the 4 molecules was performed with the results displayed in Figure 2b-e. The STM images additionally provide a good visual representation of the initial density on the basal plane. Every

bright feature in the images b-e visualizes a site of covalent attachment, though it is presently unclear whether such features necessarily correspond to a single molecule. The observed density also varies significantly for the different functional groups. In accordance with the Raman data, we find for 3,5-TBD-G and 3,4,5-TMeOD-G (Figures 2f and 2h), covalently modified surfaces that appear almost fully closed; the underlying HOPG surface is only visible through small pores in the molecular layer. On the other hand, 3,4,5-TMeD-G (Figure 2g) and especially 4-NBD-G (Figure 2i) display a distinctively lower degree of functionalization, though with this being significantly higher for 3,4,5-TMeD-G than for 4-NBD-G. This agreement between the Raman and STM is promising, as although Raman analysis remains the method of choice for quantitative analysis of defect concentrations in graphitic materials at the ensemble level, STM can additionally detail local qualitative differences that may exist at the molecular scale. Taken together, the Raman and STM data show good agreement with the findings of reference[36], although in the present case, the value for 3,5-TBD-G is in fact slightly higher (though very similar to) than 3,4,5-TMeOD-G.

Finally, representative AFM images for each system are in turn presented in Figures 2b-e. In contrast to both STM and Raman, the apparent topological appearance of all samples is rather similar, with the occasional presence of small circular “ungrafted” areas without molecules observed solely for the 4-NBD-G sample. Apart from these areas, all HOPG samples are completely covered by a uniform layer of molecules, despite the underlying discrepancies in the degree of covalent modification between these systems.

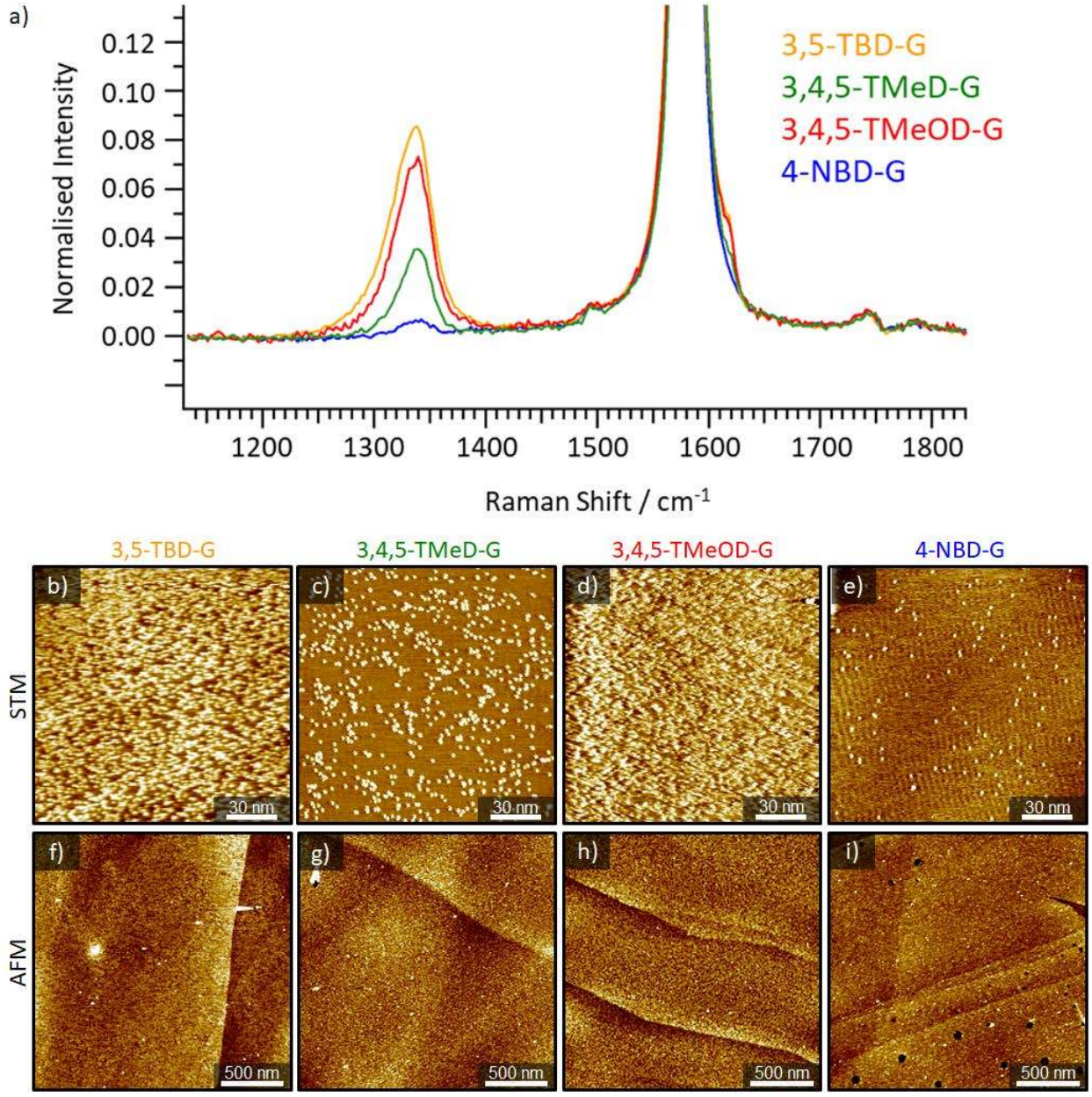

Figure 2. (a) Typical Raman spectra for the functionalized HOPG samples at room temperature, focused on the 1200-1800 cm^{-1} spectral region. For clarity, the spectra have been normalized to the value of the G-band and a polynomial (3rd order) fitted to remove the background. STM and AFM images of (b, f) 3,5-TBD-G, (c, g) 3,4,5-TMeD-G, (d, h) 3,4,5-TMeOD-G and (e, i) 4-NBD-G. Imaging parameters (STM): (b) I_{set} = 40 pA, V_{bias} = -1.2 V, (c) I_{set} = 60 pA, V_{bias} = -0.8 V, (d)

I_{set} = 50 pA, V_{bias} = -0.8 V, (e) I_{set} = 40 pA, V_{bias} = -1.0 V. Data were recorded under ambient conditions and at room temperature. The wavy features in e) are tentatively attributed to self-assembled alkane-type contaminants.

Sequential heating experiments. Sequential heating was then performed to investigate the behaviour and stability of each system at elevated temperatures. This proceeded by successively heating the samples in 10 degree temperature stages between 160 and 200 °C. Samples were heated and then held for 30 minutes at each temperature stage, before being cooled to room temperature for characterisation by Raman and SPM. The samples were thereafter returned for heating to the next stage (10 degrees higher) in the series. Further details on the procedure used can be found in the experimental methods.

The results of the Raman analysis are displayed in Figure 3a. Here the I_D/I_G is given for each heating stage, normalised to the value at room temperature to account for the intrinsic differences in starting defect density discussed in the context of Figure 2. For each molecule, a clear reduction in the value of I_D/I_G is apparent from the graph, and is attributed to a loss of covalently bound molecules upon heating. Starting with the 3,5-TBD-G sample, I_D/I_G falls to 20% of its starting value upon heating to 160 °C, with the bond almost eliminated entirely from 170 °C onwards (reduced to ~3 % of starting value). A similar I_D/I_G was found at 180 °C, before the D Band apparently falls beneath our Raman detection limit at 190 °C. In contrast, both 4-NBD-G and 3,4,5-TMeD-G show only small changes upon heating to 160 °C, whereas the behavior of 3,4,5-TMeOD-G is intermediate, showing a decrease to 60% of its starting value at 160 °C. The subsequent trend thereafter for these 3 systems is again rather similar, with I_D/I_G decreasing further at higher temperature stages, though this is less perceptible for 4-NBD-G due to the large error

bars (likely resulting from the low starting defect concentration). Taken more generally, the Raman data show that the great majority of bond breaking occurs below 200 °C regardless of the substituent. Beyond this initial finding, the results also point to some secondary dependence on the nature of the substituents of the phenyl ring in the aryldiazonium cation.

Further evidence for the changes taking place on the surface are provided through the SPM analysis. For clarity we only provide images for two molecules in the main text. Figures 3b-c and 3d-e show representative AFM and STM images at each of the measured temperature stages for 3,4,5-TMeOD-G and 3,5-TBD-G functionalized surfaces, respectively. A more complete data set is provided for each of the molecules in the Supporting Information for both AFM (Figures S2-S5) and STM (Figures S6-S9). As before, the series of STM images in Figures 3c and e are in agreement with the results from the Raman analysis; we can conclude that both samples undergo detachement of the aryl groups, starting at least by the lowest temperature studied (160 °C). This finding was further corroborated for all of the molecules in the Supporting Informtation. Nevertheless, as with Raman spectroscopy there are clear discrepancies between the different systems. Although for 3,4,5-TMeD-G (Figure S7) and 4-NBD-G (Figure S9) the first step of 160 °C shows very little detachement of molecules, we find substantial detachment for 3,4,5-TMeOD-G (Figure 3c) and even more for 3,5-TBD-G (Figure 3e). Again, this is in broad, qualitative agreement with the Raman results in Figure 3a. For 3,4,5-TMeD-G the onset of wide-spread bond breaking is found at around 170 °C and for 4-NBD-G at around 180 °C (though in both cases some reduction was already observed by 160 °C). Additionally, when the temperature treatment finishes the fifth 30 min cycle at 200 °C, practically all molecules are detached from the sample surface in all cases, with only a few isolated molecules being present in individual STM images. One should note that apparent yield of desorption appears to follow the pattern for surface coverage, with more

bonds breaking at lower temperatures for the systems that exhibited a higher degree of covalent functionalization. Quite unexpectedly, the aryl radicals that generate the greatest modification appear to be most easily desorbed. An inspection of the STM panels in Figure 3 does however indicate that this is not a direct correlation, with the STM images showing a much higher number of bonds breaking for 3,5-TBD-G than 3,4,5-TMeOD-G at 160 °C, despite there being only a small change in starting concentration.

Taken together with the Raman data, the STM analysis conclusively shows breaking of the covalent linkages at temperatures below 200 °C. This is very low for a standard C-C bond,[40] suggesting that the covalent attachment of the molecules is relatively unstable. Moreover, this is in line with previous observations that these aryl moieties are easily removed (and the graphitic lattice restored) by STM scanning.[18,41,42] However, elevated temperatures lead to this restoration occuring globally and thus not being limited to the area scanned by the STM ($< 1\ \mu m^2$).

Next, we turn to the AFM images provided in Figures 3b and d. Here, the samples undergoing the stepwise heating exhibit two distinct topological behaviours. Taking the evolution in Figure 3b as representative, a limited structural transformation for the 3,4,5-TMeD-G, 3,4,5-TMeOD-G and 4-NBD-G samples is found, with “cavities” (seen as the dark regions in Figure 3b) starting to appear from 160 °C, suggesting little loss of material from the surface. In sharp contrast, Figure 3d details very different behavior for 3,5-TBD-G, where much larger domains can be seen between regions of differing contrast. Over the course of the heating treatment these structures ripen, increasing the size and sharpness of the edge structures. The regions of high and low contrast may correspond to aggregated breakdown products and the bare HOPG surface, respectively, although conclusive chemical identification is not possible simply from differences in contrast. More importantly, both series of AFM images suggest that even in the case of the 3,5-TBD-G sample,

most of the molecular layer remains on the surface at 200 °C, whereas STM and Raman evidenced that nearly all the grafted species are detached from the surface at this temperature. Consequently, our results show that breakdown products remain physisorbed on HOPG even after covalent bond breaking has taken place.

It is of note to compare our general findings to previous studies on the thermal stability of chemically functionalized carbon systems. Firstly, several previous studies appear to indicate mass loss occurring at higher temperatures than those observed here. X-ray photoelectron spectroscopy (XPS) and Fourier-transform Infra-red (FTIR) spectroscopy show that NO_2 still resides on the surface following vacuum annealing of a 4-NBD functionalized epitaxial graphene surface to 200 °C,[22] and UHV-STM experiments have shown material present on the surface after annealing to 500 °C.[42] Additionally, TGA has pointed to hydrogen evolution from hydrogenated graphene flakes only occurring at temperatures upwards of 400 °C.[29] In contrast, previous studies using Raman spectroscopy have yielded markedly different results. Bond-breaking for hydrogenated graphene was reported to occur between 100 °C and 200 °C.[43] CNTs covalently functionalized using diazonium chemistry could be restored to their pristine state by heating to 300 °C.[26] Finally, it has been shown that graphene flakes in solution functionalized on both sides by alkyl groups show significant detachment below 200 °C.[30]

The present work helps to rationalize such differing behavior (even in light of the vastly different systems studied) by illustrating that surface desorption most likely occurs in two distinct stages. By both STM and Raman we see bond breaking largely occurring below 200 °C, whilst AFM shows that the physisorbed products remain on the surface, presumably up to the higher temperatures found by the other methods mentioned in the previous paragraph.[29,42] Indeed, this agreement between STM and Raman highlights a further point. As the lack of D band in the Raman

spectrum, indicative of a pristine sp^2 surface, is in agreement with the loss of covalently bound molecules by STM (with both being virtually absent for 3,5-TBD-G at 200 °C), it follows that the relatively low temperatures involved here are sufficient to return the surface to its pristine sp^2-hybridised state without undergoing secondary reaction.

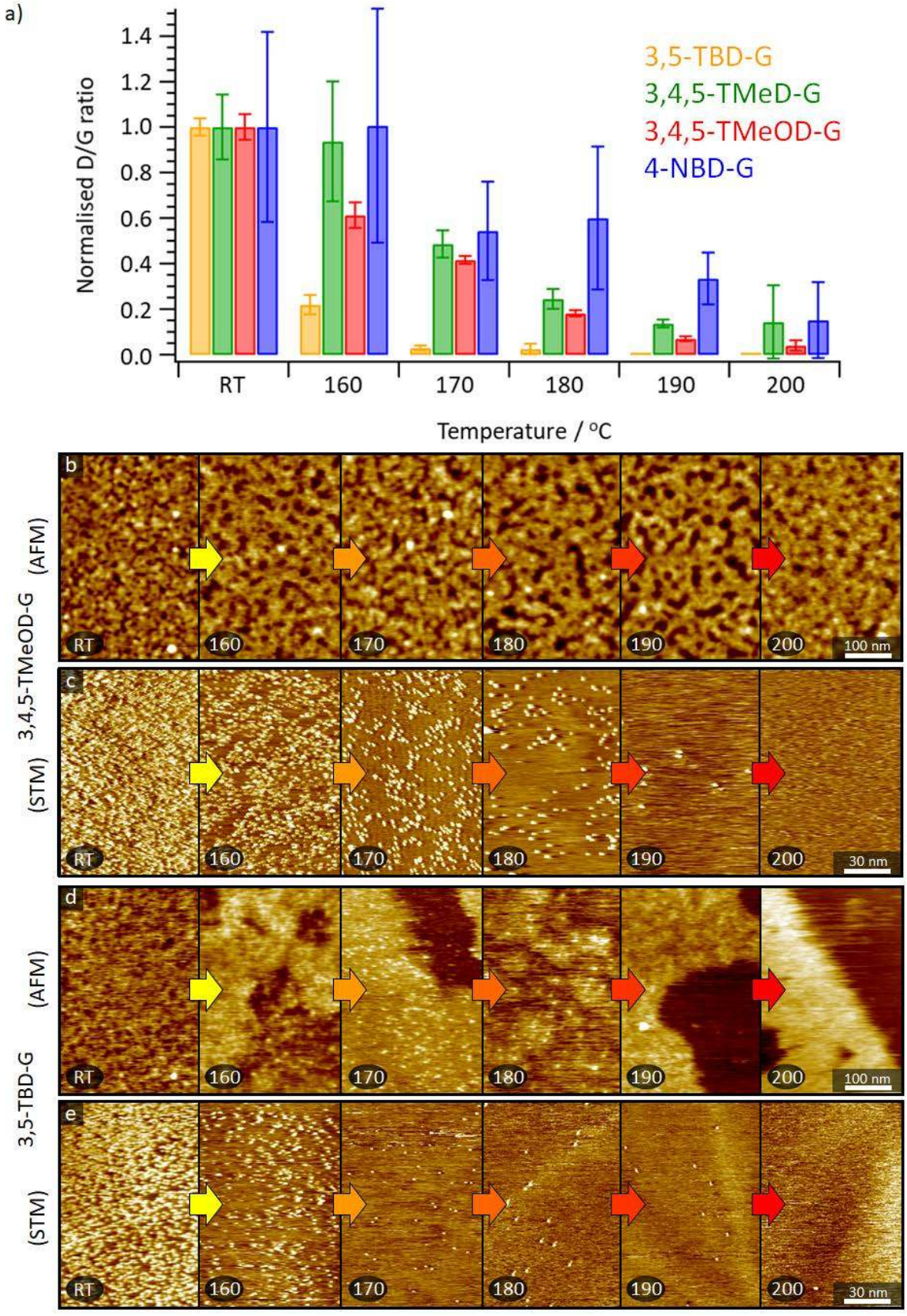
a)
Normalised D/G ratio
1.4
1.2
1.0
0.8
0.6
0.4
0.2
0.0
RT
160
170
180
190
200
Temperature / °C
3,5-TBD-G
3,4,5-TMeD-G
3,4,5-TMeOD-G
4-NBD-G
b
(AFM)
3,4,5-TMeOD-G
c
(STM)
d
(AFM)
3,5-TBD-G
e
(STM)
RT
160
170
180
190
200
100 nm
30 nm

Figure 3. (a) Raman (D/G) ratio for the 4 functionalized HOPG samples used in this study following sequential heating up to the given temperature, normalized to the value at room temperature. (b) AFM and (c) STM images of the 3,4,5-TMeOD-G system undergoing the five stages of a 30-minute stepwise heat treatment from 160 °C to 200 °C. (d) AFM and (e) STM images of the 3,5-TBD-G system undergoing a stepwise heat treatment from 160 °C to 200 °C. Imaging parameters (STM): (c) I_{set} = 50 pA, V_{bias} = -0.8 V at RT, I_{set} = 40 pA, V_{bias} = -0.8 V at 160 °C, I_{set} = 40 pA, V_{bias} = -1.1 V at 170 °C to 190 °C, I_{set} = 40 pA, V_{bias} = -1.0 V at 200 °C, (e) I_{set} = 40 pA, V_{bias} = -1.2 V at RT, I_{set} = 30 pA, V_{bias} = -1.3 V at 160 °C, I_{set} = 40 pA, V_{bias} = -1.0 V at 170 °C to 200 °C. Complete SPM data (including images for 3,4,5-TMeD-G and 4-NBD-G) can be found in Supporting Information (S2-S5, S7-S10). Data were recorded under ambient conditions and at room temperature.

Desorption kinetics. Motivated by the reduction in the defect density following sequential heating, additional Raman measurements were then performed to extend our work to a study of the kinetics of this process. It is known that the average inter-defect distance can be associated with the (D/G) value using the following phenomenological model:[39,44]

$$\frac{I_D}{I_G} = C_A \frac{(r_A^2 - r_S^2)}{(r_A^2 - 2r_S^2)} \left[e^{-\pi r_s^2 / L_D^2} - e^{-\pi (r_A^2 - r_S^2)/L_D^2} \right] + C_S \left[1 - e^{-\pi r_S^2 / L_D^2} \right] \quad (1)$$

Here r_s is a length scale corresponding to the size of the introduced point defects, with r_A defining a surrounding "activated" region within which D band generation becomes possible. Typical values for r_A and r_S are 1 nm and 3 nm, respectively. In turn, L_D, defines the average distance between defects, with C_S and C_A being constants. The model works by considering only electron-hole pairs generated within the region surrounding a defect (and defined by r_A rather than r_s) as capable of generating a D band. Consequently, two regimes are defined, with the D band first

increasing for increasing defect concentration up to a point where defective regions coalesce and the average inter-defect distance approaches the difference between r_s and r_A. After this point, the I_D/I_G subsequently decreases for higher defect concentrations. Accordingly, in the low defect regime equation 1 can be reduced to the familiar Tuinstra-Koenig relation:[37,44]

$$\frac{I_D}{I_G} \cong \frac{\pi C_A (r_A^2 - r_s^2)}{L_D^2} \quad (2)$$

As the present case involves point defects, this can in turn be related to the defect density (and hence the concentration of molecules, σ, covalently bound to the surface) such that:

$$\frac{I_D}{I_G} \propto \frac{1}{L_D^2} \propto \sigma \quad (3)$$

The above discussion was largely based on defects formed through ion-bombardment but is also known to apply for defects on graphene following covalent attachment, as studied here. Indeed, r_s, and consequently the defect concentration at which I_D/I_G maximizes may have some dependence on the defect type.[45,46] In this case, the transition between the two stages may occur at higher concentrations for the single-atom point defects involved in the present study. Moreover, while the high-defect regime can be reached through the covalent-type point defects on graphene, I_D/I_G saturates at a fixed level for ion-bombardment type defects on graphite.[41] Such saturation of I_D/I_G was also seen for covalent-type defects on graphite.[18] However, this was found to occur at higher values and diazonium concentrations than were used in this study, suggesting that we remain in the low defect regime. Moreover, to the best of our knowledge I_D/I_G has never been seen to decrease following saturation for molecules covalently bound to graphite. It may be the case that steric considerations prevent the high defect regime from ever being reached in such systems as those studied here. As such, we make the assumption that the low-density regime persists throughout the measurements performed here, and that the relationship defined in equation 3 is valid.

Relative changes to the concentration of covalently bound molecules over time were extracted by monitoring changes in the normalized I_D/I_G value at constant temperature and under controlled environment. This was then used to calculate the rate constant for the thermally induced fission of the aryl-graphene bond:

$$-\frac{d\sigma}{dt} = \sigma k = -\frac{d\frac{I_D}{I_G}}{dt} \quad (4)$$

Assuming an Arrhenius type temperature dependence of the rate constant *k* and making multiple measurements at different temperatures then allows the activation energy and pre-exponential factor for bond breaking to be extracted. Further details on the procedure used to evaluate the reaction kinetics are given in the experimental methods. Average starting I_D/I_G values at room temperature varied slightly from the case of sequential heating, and were around 0.09 for 3,4,5-TMeOD-G, 0.1 for 3,5-TBD-G and 0.05 for 3,4,5-TMeD-G. Due to its low I_D/I_G ratio starting value, 4-NBD-G was not included in this study.

Figure 4 shows a graph of the natural logarithm, *ln(k)*, of the rate constant against the inverse temperature, 1/T, for the 3,4,5-TMeOD-G, 3,5-TBD-G and 3,4,5-TMeD-G systems. In each case a linear fit of the data to the linearized Arrhenius equation $ln(k) = ln(A) - E_a/RT$, is also provided, with A and E_a being the pre-exponential factor and the activation energy, respectively. In all three cases, the fit suggests a reasonable agreement of the data with the Arrhenius equation. Both the 3,4,5-TMeOD-G and 3,4,5-TMeD-G systems show very similar behavior, whereas for 3,5-TBD-G a much steeper dependence on temperature is observed. One should note that a greater variability was observed for 3,5-TBD-G where, for a given temperature, the data could vary substantially. This was at the single measurement level, and not specifically related to a particular measurement session (Figure S11). It is also worth emphasizing here that to maximize time-resolution, spectra

were only recorded at a single position for each sample, though this doesn't account for thermal drift. Full rate constant data can be found in the supporting information (table S2).

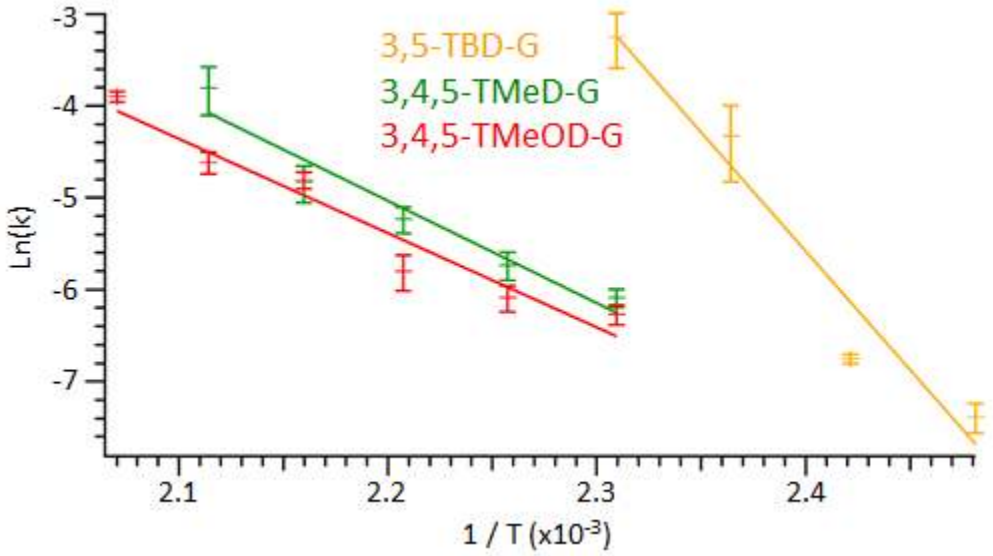

Figure 4. Desorption kinetics. Graph showing the natural logarithm of the rate constant for the thermal fission of the aryl-HOPG bond, plotted against inverse temperature for 3,5-TBD-G, 3,4,5-TMeD-G and 3,4,5-TMeOD-G. In each case, a linear fit to the data is provided.

Table 1 displays the relevant fit parameters taken from each of these fits. Extracting the activation energy for the thermal fission of the aryl-graphene bond from the gradient of the slopes in Figure 4 yields values of around ~90 ± 10 kJ mol^{-1} (0.9 ± 0.1 eV/ 20 ± 2 kcal mol^{-1}) and ~90 ± 10 kJ mol^{-1} (1.0 ± 0.1 eV / 22 ± 3 kcal mol^{-1}) for 3,4,5-TMeOD-G and 3,4,5-TMeD-G, respectively. In contrast, the activation energy for 3,5-TBD-G was found to be around ~210 ± 40 kJ mol^{-1} (2.2 ± 0.4 eV / 51 ± 8 kcal mol^{-1}). Also included is data on the entropy and enthalpy of reaction, $\Delta S^{\ddagger}$ and $\Delta H^{\ddagger}$ as obtained from the analysis of the data in the framework of the Eyring equation (Figure S10) and discussed below.

Table1. Extracted reaction data for 3,4,5-TMeOD, 3,4,5-TMeD and 3,5-TBD functionalized HOPG surfaces.

Aryldiazonium salts used for functionalization	Activation energy (kJ mol^{-1})	Pre-exponential factor	$\Delta S^{\ddagger}$ (J mol^{-1} K^{-1})	$\Delta H^{\ddagger}$ (kJ mol^{-1})
3,5-TBD-G	210 ± 40	3×10^{24} ($10^{20} – 10^{28}$)	210 ± 40	210 ± 40
3,4,5-TMeD-G	90 ± 10	3×10^{8} ($10^{6} – 10^{10}$)	-100 ± 30	90 ± 10
3,4,5-TMeOD-G	90 ± 10	3×10^{7} ($10^{6} – 10^{8}$)	-110 ± 30	80 ± 10

It may be expected that 3,4,5-TMeD-G shows a higher activation energy than 3,4,5-TMeOD-G, as it is seen to leave at higher temperatures and may provide weaker radical stabilization through the absence of methoxy groups. However, any difference between the values obtained for 3,4,5-TMeOD-G and 3,4,5-TMeD-G appears to fall beneath the sensitivity of the method used here. Both values also agree reasonably with theoretical calculations (100-125 kJ mol^{-1}) for a graphene sheet covalently functionalized with aryls at full surface coverage, (even though this value may have been underestimated since the van der Waals contribution was not considered).[47] This highlights once again the relative weakness of the bond compared to a standard C-C linkage

(determined as ~ 410 kJ mol^{-1} / 4.3 eV for a phenyl – $C(CH_3)_3$ bond).[40] At first glance this is a surprising result, however, this weakness is reflective of the nature of the bond, with each sp^3 carbon "pulled" out of the lattice by around 0.7 Å.[47] Covalent functionalization therefore induces significant strain in the lattice and precludes full relaxation into a typical tetrahedral configuration. The strain also explains why the fission of the aryl-HOPG bond occurs at lower temperature than for graphene flakes functionalized on both sides.[30,40] As opposed to one-side functionalization ("*supratopic*"), double-side functionalization of graphene ("*antaratopic*") can lead to strain-free, more stable structures.[48]

The much greater value of the activation energy found for 3,5-TBD-G is unexpected when cognizant of its tendency for bond-breaking at significantly lower temperature than any other system used in this study and it is interesting that the AFM results of Figure 3 also distinguish this system from the others studied. Tests using a second-order kinetics model to describe the time and temperature dependence of I_D/I_G did not appear to yield better fittings for the rate constants (Supporting Information) and it was therefore decided to keep a first-order model given the small temperature range used. Moreover, given the similarities in electron donating properties of the substituents in 3,5-TBD and 3,4,5-TMeD, an intrinsic chemical effect also seems unlikely to explain the observed trend and may suggest some steric influence of the bulky *tert*-butyl groups on 3,5-TBD.

A large pre-exponential factor (10^{24} s^{-1}) explains the paradox between the fast dissociation rate and the large activation barrier, and more information is provided by a further analysis in the context of the Eyring approach ($k \approx kT/\hbar exp(\Delta S^{\ddagger}/Rexp(\Delta H^{\ddagger}/RT))$. Here, one obtains for 3,4,5-TMeD-G and 3,4,5-TMeOD-G samples, respectively -100 ± 30 J mol^{-1} K^{-1} and -110 ± 30 J mol^{-1} K^{-1} for the entropy of activation. For 3,5-TBD-G, on the other hand, a positive value of +210 ± 40

J mol^{-1} K^{-1} is obtained. This positive value of $\Delta S^{\ddagger}$ is in line with the expectations for the dissociation of a bond. This suggests that for 3,5-TBD-G the dissociation of the covalent bond leads to the desorption of 3,5-*tert*-butylphenyls. The outspoken negative values of $\Delta S^{\ddagger}$ for 3,4,5-TMeOD-G and 3,4,5-TMeD-G are in fact quite unexpected for a reaction corresponding essentially to the dissociation of a bond. This suggests that already in the transition state the newly formed radical starts to adsorb to the HOPG surface or to interact with other defect centers, other adsorbed molecules, or indeed any other species present on the surface. Both systems were also tested using second order kinetics as a result of these findings, but this didn't appear to yield significantly improved fittings (Figure S13-S14) and did not yield large changes to the results. We hope further investigations will elucidate in more detail the mechanism responsible for the difference in behavior between 3,5-TBD-G and the other two systems.

This notwithstanding, our results from this kinetics study highlight how using Raman scattering to probe the aryl-graphene bond can provide information not accessible through other techniques, such as TGA, that indirectly measure the bond strength by detecting mass loss from the surface. The similarities between experiment and theory for 3,4,5-TMeOD-G and 3,4,5-TMeD-G help to validate the method for directly accessing bond strengths of chemically functionalized graphitic surfaces. As such, it opens the way for further studies investigating how bond and surface properties are influenced by factors such as lattice strain, molecular arrangement or the nature of substituents, on graphite and other 2D carbon surfaces.

Conclusions

In this work, we have used a combination of scanning probe microscopies and Raman spectroscopy to study the temperature evolution of HOPG surfaces covalently modified through

arenediazonium chemistry. The complementarity between Raman, STM (following the local degree of functionalization) and AFM (monitoring physical changes to the surface) allows the desorption process to be deconvoluted, showing that on this surface the bond between aryl moieties and HOPG breaks below 200 °C, after which the breakdown products largely remain physisorbed. Raman spectroscopy offers a simple and quick way to obtain ensemble results on this bond breaking, as well as to study its kinetics. These three techniques shed new light on the thermal desorption of aryl groups attached to carbon surfaces, complementing the knowledge gathered previously with thermogravimetric analysis.

Besides this, the work presented here establishes a general method for determining the thermal kinetics of covalently functionalized carbon-based systems and accessing the activation energy of the bond cleavage. It shows the bond formed following covalent functionalization to be substantially weaker (between 90 and 210 $kJmol^{-1}$) than a standard C-C linkage, likely due to the strain induced by the sp^2 to sp^3 rehybridization, and moreover highlights some interesting substituent-based effects. While the large pre-exponential factor and positive value of $\Delta S^{\neq}$ obtained for the dissociation of 3,5-TBD-G are compatible with bond dissociation and consequent desorption, the corresponding values obtained for 3,4,5-TMeD-G and 3,4,5-TMeOD-G suggest a more complex mechanism with a lower activation barrier that appears to more closely agrees with previous theoretical calculations. For 3,5-TBD-G this mechanism is probably impeded due to steric repulsion. The limited stability of the covalent bond formed permits the restoration of the pristine HOPG lattice at relatively low temperature, opening the way to defect-free functionalization and post-modification of sp^2-hybridized carbon allotropes such as graphene. On the other hand, it also raises questions over potential thermal operating windows for future applications.

By using HOPG, the simplest and most well understood carbon-based system, a baseline has been established for further investigations into more diverse and complex systems. This method can be potentially applied to arbitrary moieties chemisorbed on graphite, as well as to patterned functionalization. It can also be extended to other surfaces such as surface-supported graphene or two-side functionalized graphene in order to compare and quantify their stability. These initial findings also call for further detailed experimental and theoretical investigations into the reaction pathway(s) of the bond cleavage.

Supporting Information

The Supporting Information is available free of charge on the ACS Publications website.

Cyclic voltammograms of the grafting of the four molecules; AFM data and STM images of the stepwise heating of the four samples; Detailed analysis of the desorption kinetics.

Author information

Corresponding author. *E-mail: steven.defeyter@kuleuven.be.

Acknowledgment

This work is supported by the Fund of Scientific Research–Flanders (FWO), KU Leuven – Internal Funds, and European Research Council under the European Union's Seventh Framework Programme (FP7/2007– 2013)/ERC Grant Agreement No. 340324. We also thank We thank Dr. Kunal Mali for stimulating discussions.

References

(1) Hirsch, A. The Era of Carbon Allotropes. *Nat. Mater.* **2010**, *9* (11), 868–871.

(2) Prato, M. Fullerene Chemistry for Materials Science Applications. *J. Mater. Chem.* **1997**, *7* (7), 1097–1109.

(3) Prato, M.; Maggini, M. Fulleropyrrolidines: A Family of Full-Fledged Fullerene Derivatives. *Acc. Chem. Res.* **1998**, *31* (9), 519–526.

(4) Bahr, J. L.; Yang, J.; Kosynkin, D. V.; Bronikowski, M. J.; Smalley, R. E.; Tour, J. M. Functionalization of Carbon Nanotubes by Electrochemical Reduction of Aryl Diazonium Salts: A Bucky Paper Electrode. *J. Am. Chem. Soc.* **2001**, *123* (27), 6536–6542.

(5) Georgakilas, V.; Kordatos, K.; Prato, M.; Guldi, D. M.; Holzinger, M.; Hirsch, A. Organic Functionalization of Carbon Nanotubes. *J. Am. Chem. Soc.* **2002**, *124* (5), 760–761.

(6) Hudson, J. L.; Casavant, M. J.; Tour, J. M. Water-Soluble, Exfoliated, Nonroping Single-Wall Carbon Nanotubes. *J. Am. Chem. Soc.* **2004**, *126* (36), 11158–11159.

(7) Georgakilas, V.; Otyepka, M.; Bourlinos, A. B.; Chandra, V.; Kim, N.; Kemp, K. C.; Hobza, P.; Zboril, R.; Kim, K. S. Functionalization of Graphene: Covalent and Non-Covalent Approaches, Derivatives and Applications. *Chem. Rev.* **2012**, *112* (11), 6156–6214.

(8) Dennler, B. G.; Scharber, M. C.; Brabec, C. J. Polymer - Fullerene Bulk - Heterojunction Solar Polymer-Fullerene Bulk-Heterojunction Solar Cells. *Adv. Mater.* **2009**, *21* (13), 1323–1338.

(9) Coleman, J. N.; Khan, U.; Gun'ko, Y. K. Mechanical Reinforcement of Polymers Using Carbon Nanotubes. *Adv. Mater.* **2006**, *18* (6), 689–706.

(10) Liu, Y.; Dong, X.; Chen, P. Biological and Chemical Sensors Based on Graphene Materials. *Chem. Soc. Rev.* **2012**, *41* (6), 2283–2307.

(11) Diederich, F.; Gómez-López, M. Supramolecular Fullerene Chemistry. *Chem. Soc. Rev.*

1999, *28* (5), 263–277.

(12) Tasis, D.; Tagmatarchis, N.; Bianco, A.; Prato, M. Chemistry of Carbon Nanotubes. *Chem. Rev.* **2006**, *106* (3), 1105–1136.

(13) Mali, K. S.; Greenwood, J.; Adisoejoso, J.; Phillipson, R.; De Feyter, S. Nanostructuring Graphene for Controlled and Reproducible Functionalization. *Nanoscale* **2015**.

(14) Fan, X. Y.; Nouchi, R.; Yin, L. C.; Tanigaki, K. Effects of Electron-Transfer Chemical Modification on the Electrical Characteristics of Graphene. *Nanotechnology* **2010**, *21* (47), 475208.

(15) Pembroke, E.; Ruan, G.; Sinitskii, A.; Corley, D. A.; Yan, Z.; Sun, Z.; Tour, J. M. Effect of Anchor and Functional Groups in Functionalized Graphene Devices. *Nano Res.* **2013**, *6* (2), 138–148.

(16) Delamar, M.; Hitmi, R.; Pinson, J.; Savéant, J. Covalent Modification of Carbon Surfaces by Grafting of Functionalized Aryl Radicals Produced from Electrochemical Reduction of Diazonium Salts. *J. Am. Chem. Soc.* **1992**, *114* (14), 5883–5884.

(17) Pinson, J.; Podvorica, F. Attachment of Organic Layers to Conductive or Semiconductive Surfaces by Reduction of Diazonium Salts. *Chem. Soc. Rev.* **2005**, *34* (5), 429–439.

(18) Greenwood, J.; Phan, T. H.; Fujita, Y.; Li, Z.; Ivasenko, O.; Vanderlinden, W.; Van Gorp, H.; Frederickx, W.; Lu, G.; Tahara, K.; et al. Covalent Modification of Graphene and Graphite Using Diazonium Chemistry: Tunable Grafting and Nanomanipulation. *ACS Nano* **2015**, *9* (5), 5520–5535.

(19) Criado, A.; Melchionna, M.; Marchesan, S.; Prato, M. The Covalent Functionalization of Graphene on Substrates. *Angew. Chemie - Int. Ed.* **2015**, *54* (37), 10734–10750.

(20) Bélanger, D.; Pinson, J. Electrografting: A Powerful Method for Surface Modification.

Chem. Soc. Rev. **2011**, *40* (7), 3995–4048.

(21) Mahouche-Chergui, S.; Gam-Derouich, S.; Mangeney, C.; Chehimi, M. M. Aryl Diazonium Salts: A New Class of Coupling Agents for Bonding Polymers, Biomacromolecules and Nanoparticles to Surfaces. *Chem. Soc. Rev.* **2011**, *40* (7), 4143–4166.

(22) Bekyarova, E.; Itkis, M. E.; Ramesh, P.; Berger, C.; Sprinkle, M.; De Heer, W. A.; Haddon, R. C. Chemical Modification of Epitaxial Graphene: Spontaneous Grafting of Aryl Groups. *J. Am. Chem. Soc.* **2009**, *131* (4), 1336–1337.

(23) Mévellec, V.; Roussel, S.; Tessier, L.; Chancolon, J.; Mayne-L'Hermite, M.; Deniau, G.; Viel, P.; Palacin, S. Grafting Polymers on Surfaces: A New Powerful and Versatile Diazonium Salt-Based One-Step Process in Aqueous Media. *Chem. Mater.* **2007**, *19* (25), 6323–6330.

(24) Allongue, P.; Delamar, M.; Desbat, B.; Fagebaume, O.; Hitmi, R.; Pinson, J.; Savéant, J. M. Covalent Modification of Carbon Surfaces by Aryl Radicals Generated from the Electrochemical Reduction of Diazonium Salts. *J. Am. Chem. Soc.* **1997**, *119* (1), 201–207.

(25) Bouriga, M.; Chehimi, M. M.; Combellas, C.; Decorse, P.; Kanoufi, F.; Deronzier, A.; Pinson, J. Sensitized Photografting of Diazonium Salts by Visible Light. *Chem. Mater.* **2013**, *25* (1), 90–97.

(26) Strano, M. S.; Dyke, C. A.; Usrey, M. L.; Barone, P. W.; Allen, M. J.; Shan, H.; Kittrell, C.; Hauge, R. H.; Tour, J. M.; Smalley, R. E. Electronic Structure Control of Single-Waited Carbon Nanotube Functionalization. *Science.* **2003**, *301* (5639), 1519–1522.

(27) Toupin, M.; Bélanger, D. Thermal Stability Study of Aryl Modified Carbon Black by in Situ Generated Diazonium Salt. *J. Phys. Chem. C* **2007**, *111* (14), 5394–5401.

(28) Dasler, D.; Schäfer, R. A.; Minameyer, M. B.; Hitzenberger, J. F.; Hauke, F.; Drewello, T.;

Hirsch, A. Direct Covalent Coupling of Porphyrins to Graphene. *J. Am. Chem. Soc.* **2017**, *139* (34), 11760–11765.

(29) Schäfer, R. A.; Englert, J. M.; Wehrfritz, P.; Bauer, W.; Hauke, F.; Seyller, T.; Hirsch, A. On the Way to Graphane - Pronounced Fluorescence of Polyhydrogenated Graphene. *Angew. Chemie - Int. Ed.* **2013**, *52* (2), 754–757.

(30) Abellán, G.; Schirowski, M.; Edelthalhammer, K. F.; Fickert, M.; Werbach, K.; Peterlik, H.; Hauke, F.; Hirsch, A. Unifying Principles of the Reductive Covalent Graphene Functionalization. *J. Am. Chem. Soc.* **2017**, *139* (14), 5175–5182.

(31) Menanteau, T.; Dias, M.; Levillain, E.; Downard, A. J.; Breton, T. Electrografting via Diazonium Chemistry: The Key Role of the Aryl Substituent in the Layer Growth Mechanism. *J. Phys. Chem. C* **2016**, *120* (8), 4423–4429.

(32) Malard, L. M.; Pimenta, M. a.; Dresselhaus, G.; Dresselhaus, M. S. Raman Spectroscopy in Graphene. *Phys. Rep.* **2009**, *473* (5–6), 51–87.

(33) Kovaříček, P.; Vrkoslav, V.; Plšek, J.; Bastl, Z.; Fridrichová, M.; Drogowska, K.; Kalbáč, M. Extended Characterization Methods for Covalent Functionalization of Graphene on Copper. *Carbon N. Y.* **2017**, *118*, 200–207.

(34) Xia, Z.; Leonardi, F.; Gobbi, M.; Liu, Y.; Bellani, V.; Liscio, A.; Kovtun, A.; Li, R.; Feng, X.; Orgiu, E.; et al. Electrochemical Functionalization of Graphene at the Nanoscale with Self-Assembling Diazonium Salts. *ACS Nano* **2016**, *10* (7), 7125–7134.

(35) Sampathkumar, K.; Diez-Cabanes, V.; Kovaricek, P.; del Corro, E.; Bouša, M.; Hošek, J.; Kalbac, M.; Frank, O. On the Suitability of Raman Spectroscopy to Monitor the Degree of Graphene Functionalization by Diazonium Salts. *J. Phys. Chem. C* **2019**, *123* (36), 22397–22402.

(36) Tahara, K.; Kubo, Y.; Lindner, B.; Hashimoto, S.; Hirose, S.; Brown, A.; Hirsch, B.; Daukiya, L.; De Feyter, S.; Tobe, Y. Steric and Electronic Effects of Electrochemically Generated Aryl Radicals on Grafting of the Graphite Surface. *Langmuir* **2019**, *35* (6), 2089–2098.

(37) Ferrari, A. C.; Basko, D. M. Raman Spectroscopy as a Versatile Tool for Studying the Properties of Graphene. *Nat. Nanotechnol.* **2013**, *8* (4), 235–246.

(38) Beams, R.; Gustavo Cançado, L.; Novotny, L. Raman Characterization of Defects and Dopants in Graphene. *J. Phys. Condens. matter* **2015**, *27* (8), 083002.

(39) Lucchese, M. M.; Stavale, F.; Ferreira, E. H. M.; Vilani, C.; Moutinho, M. V. O.; Capaz, R. B.; Achete, C. A.; Jorio, A. Quantifying Ion-Induced Defects and Raman Relaxation Length in Graphene. *Carbon N. Y.* **2010**, *48* (5), 1592–1597.

(40) Blanksby, S. J.; Ellison, G. B. Bond Dissociation Energies of Organic Molecules. *Acc. Chem. Res.* **2003**, *36* (4), 255–263.

(41) Ma, H.; Lee, L.; Brooksby, P. A.; Brown, S. A.; Fraser, S. J.; Gordon, K. C.; Leroux, Y. R.; Hapiot, P.; Downard, A. J. Scanning Tunneling and Atomic Force Microscopy Evidence for Covalent and Noncovalent Interactions between Aryl Films and Highly Ordered Pyrolytic Graphite. *J. Phys. Chem. C* **2014**, *118*, 5820–5826.

(42) Hossain, M. Z.; Walsh, M. a; Hersam, M. C. Scanning Tunneling Microscopy, Spectroscopy, and Nanolithography of Epitaxial Graphene Chemically Modified with Aryl Moieties. *J. Am. Chem. Soc.* **2010**, *132* (43), 15399–15403.

(43) Ryu, S.; Han, M. Y.; Maultzsch, J.; Heinz, T. F.; Kim, P.; Steigerwald, M. L.; Brus, L. E. Reversible Basal Plane Hydrogenation of Graphene. *Nano Lett.* **2008**, *8* (12), 4597–4602.

(44) Eckmann, A.; Felten, A.; Verzhbitskiy, I.; Davey, R.; Casiraghi, C. Raman Study on

Defective Graphene: Effect of the Excitation Energy, Type, and Amount of Defects. *Phys. Rev. B - Condens. Matter Mater. Phys.* **2013**, *88* (3), 1–11.

(45) Venezuela, P.; Lazzeri, M.; Mauri, F. Theory of Double-Resonant Raman Spectra in Graphene: Intensity and Line Shape of Defect-Induced and Two-Phonon Bands. *Phys. Rev. B - Condens. Matter Mater. Phys.* **2011**, *84* (3), 1–25.

(46) Eckmann, A.; Felten, A.; Mishchenko, A.; Britnell, L.; Krupke, R.; Novoselov, K. S.; Casiraghi, C. Probing the Nature of Defects in Graphene by Raman Spectroscopy. *Nano Lett.* **2012**, *12* (8), 3925–3930.

(47) Jiang, D. E.; Sumpter, B. G.; Dai, S. How Do Aryl Groups Attach to a Graphene Sheet? *J. Phys. Chem. B* **2006**, *110* (47), 23628–23632.

(48) Hirsch, A.; Hauke, F. Post-Graphene 2D Chemistry: The Emerging Field of Molybdenum Disulfide and Black Phosphorus Functionalization. *Angew. Chemie - Int. Ed.* **2018**, *57* (16), 4338–4354.

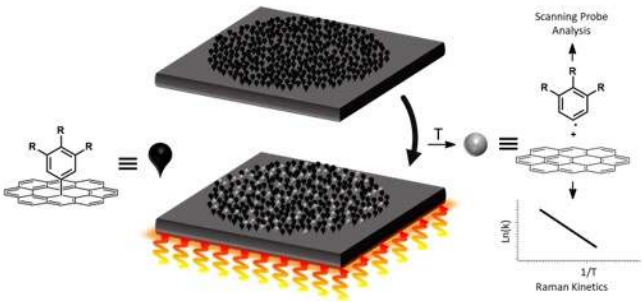

1

Supporting Information

On the Thermal Stability of Aryl Groups Chemisorbed on Graphite

Hans Van Gorp,[a‡] Peter Walke,[a‡] Joan Teyssandier,[a] Brandon E. Hirsch,[a] Hiroshi Uji-i,[ab] Kazukuni Tahara,[c] Yoshito Tobe,[de] Mark Van der Auweraer,[a] Steven De Feyter[a]*

[a] Department of Chemistry, Division of Molecular Imaging and Photonics, KU Leuven-University of Leuven, Celestijnenlaan 200F, B-3001 Leuven, Belgium.

[b] RIES, Hokkaido University, N20W10, Kita-Ward, Sapporo, Japan.

[c] Department of Applied Chemistry, School of Science and Technology, Meiji University, 1-1-1 Higashimita, Tama-ku, Kawasaki, Kanagawa, 214-8571, Japan.

[d] Division of Frontier Materials Science, Graduate School of Engineering Science, Osaka University, Toyonaka, Osaka 560-8531, Japan

[e] The Institute of Scientific and Industrial Research, Osaka University, Ibaraki, Osaka 567-0047, Japan

S1. Cyclic voltammetry

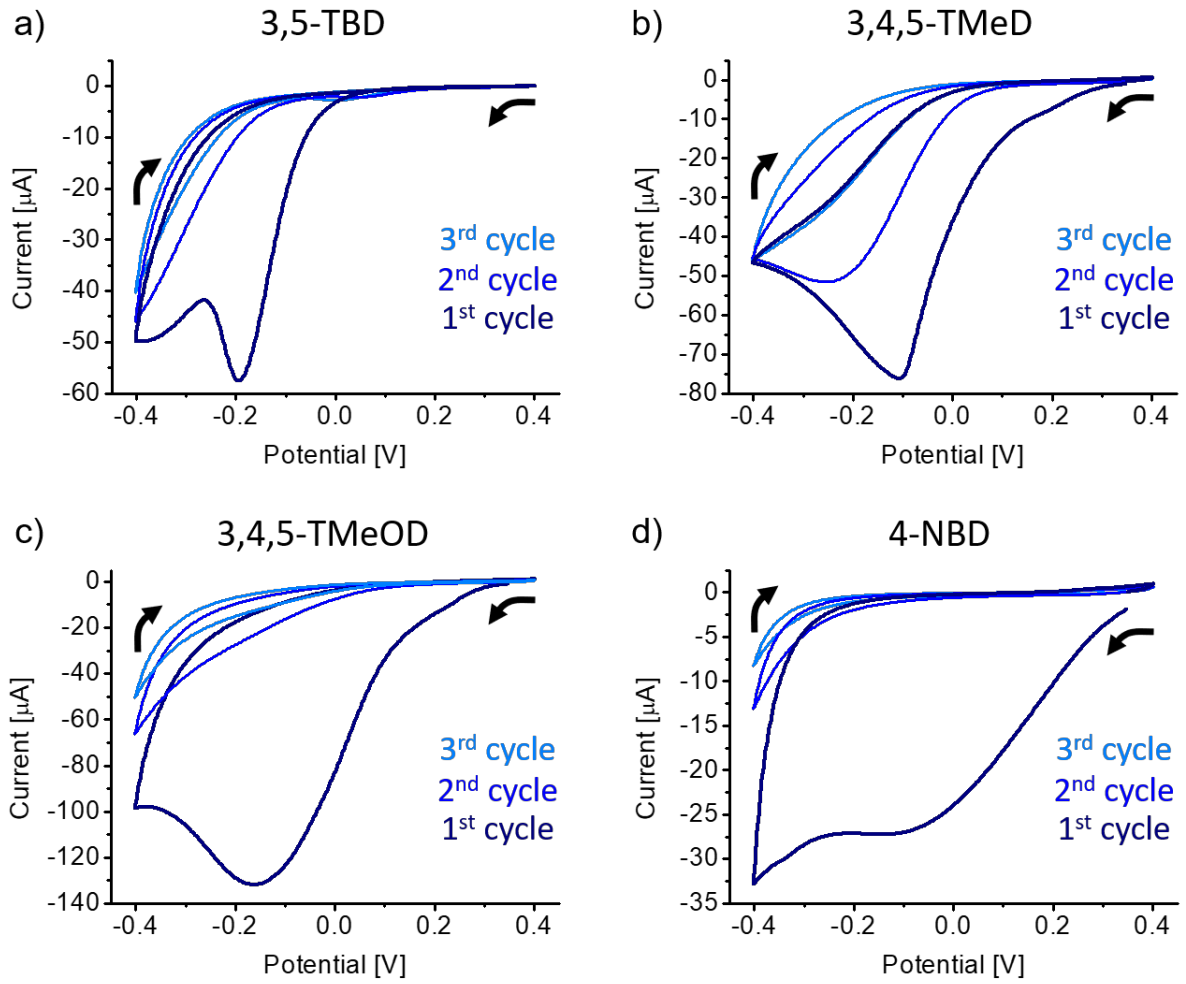

Figure S1. Cyclic voltammograms of (a) 3,5-TBD, (b) 3,4,5-TMeD, (c) 3,4,5-TMeOD and (d) 4-NBD grafting, operated in an acidic aqueous solution (HCl_{aq}, 50 mM) containing 2.0 mM of the specified constituent. Each sample undergoes three cycles of ramps in potential, starting from +0.4 V to −0.4 V, at a scan rate of 0.1 V/s. The first cycle is displayed in a dark blue with the succeeding second and third cycle presented in lighter shades of blue. Arrows illustrate the propagation of both scan directions. The first reduction wave is observed at -0.19 V for 3,5-TBD, -0.11 V for 3,4,5-TMeD, -0.16 V for 3,4,5-TMeOD and at -0.14V for 4-NBD.

S2. AFM data of stepwise heating for 3,5-TBD-G

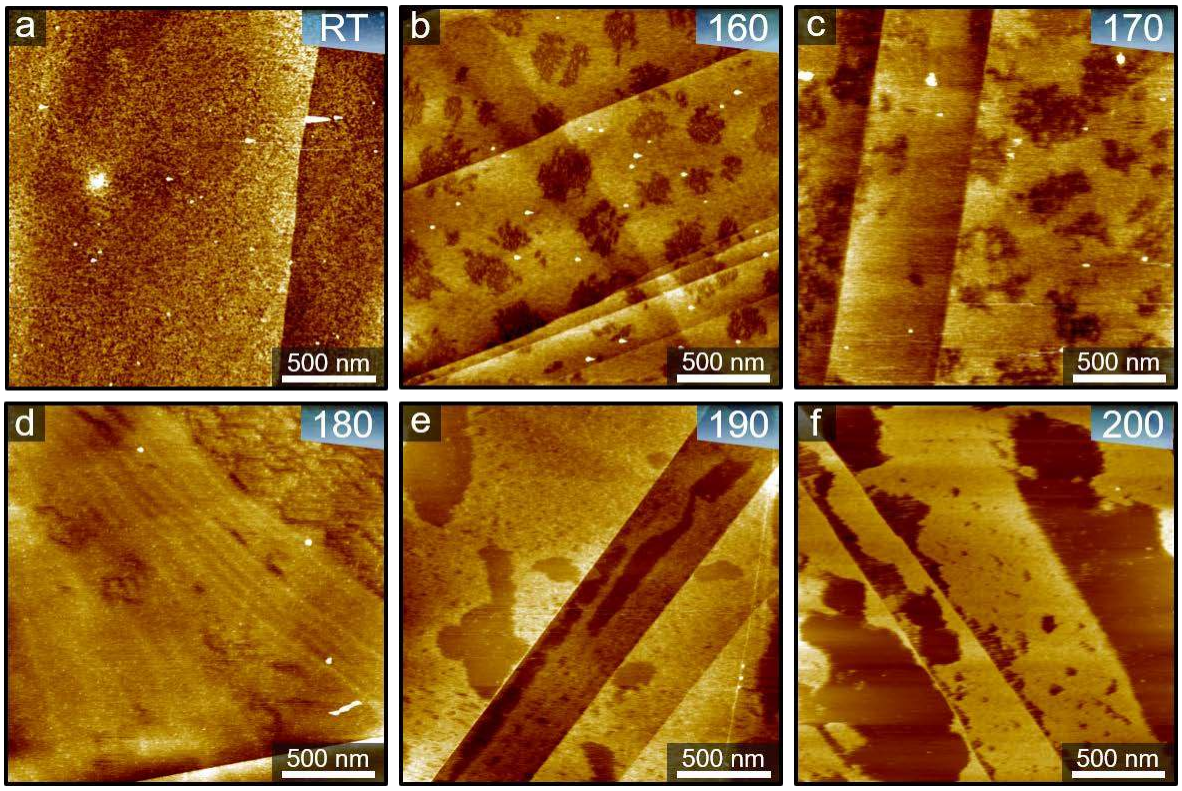

Figure S2. AFM topography images of a 3,5-TBD modified HOPG substrate at (a) room temperature, and after all stages of the stepwise heating process (b) 160 °C, (c) 170 °C, (d) 180 °C, (e) 190 °C and (f) 200 °C. The dense monolayer as observed at room temperature changes its topography substantially over the course of the temperature treatment. As the temperature increases, severe structural reform takes place differentiating clearly between the areas of breakdown products and regions of nearly bare HOPG surface.

S3. AFM data of stepwise heating for 3,4,5-TMeD-G

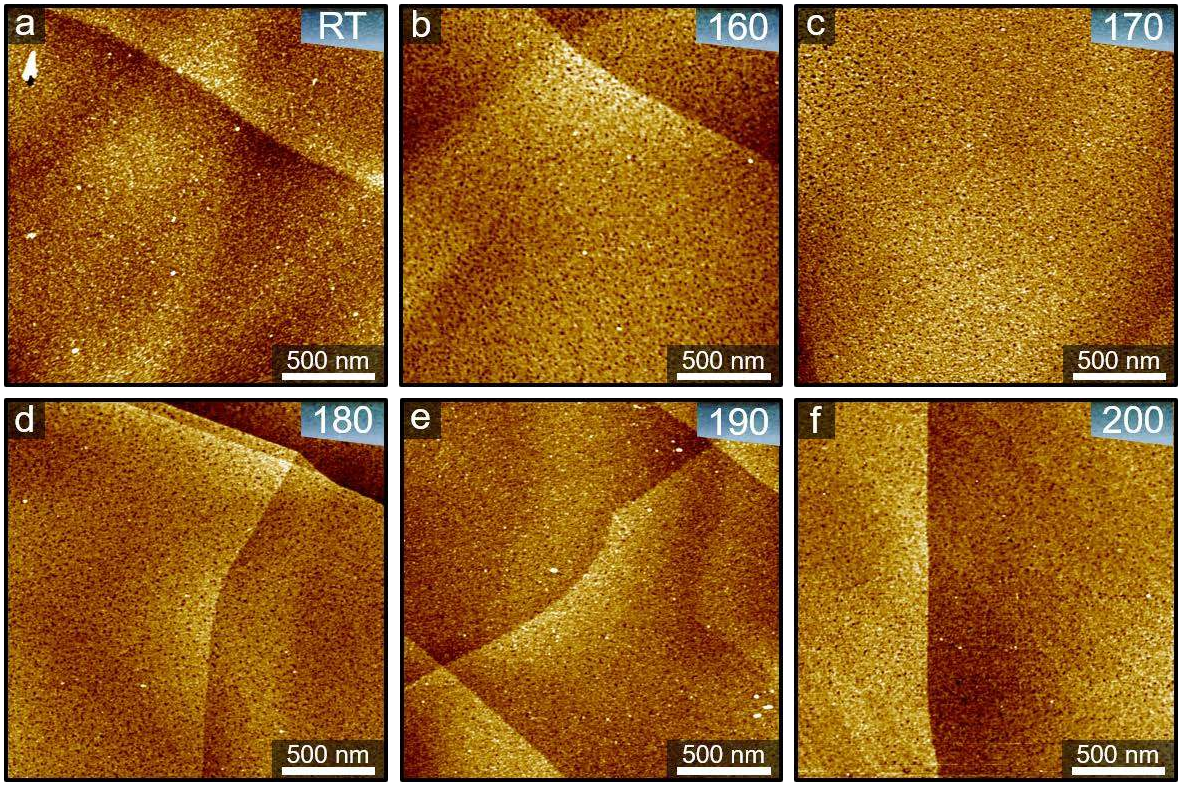

Figure S3. AFM topography images of a 3,4,5-TMeD modified HOPG substrate at (a) room temperature, and after all stages of the stepwise heating process (b) 160 °C, (c) 170 °C, (d) 180 °C, (e) 190 °C and (f) 200 °C.

S4. AFM data of stepwise heating for 3,4,5-TMeOD-G

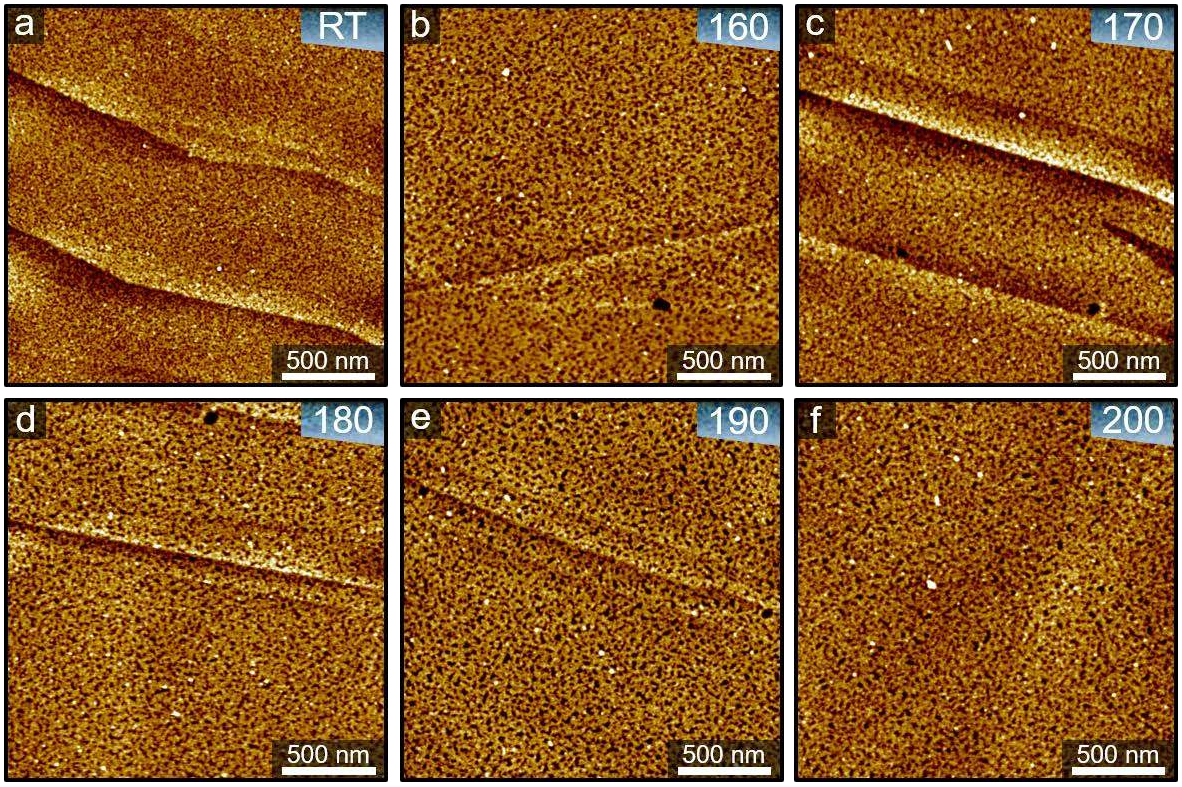

Figure S4. AFM topography images of a 3,4,5-TMeOD modified HOPG substrate at (a) room temperature, and after all stages of the stepwise heating process (b) 160 °C, (c) 170 °C, (d) 180 °C, (e) 190 °C and (f) 200 °C.

S5. AFM data of stepwise heating for 4-NBD-G

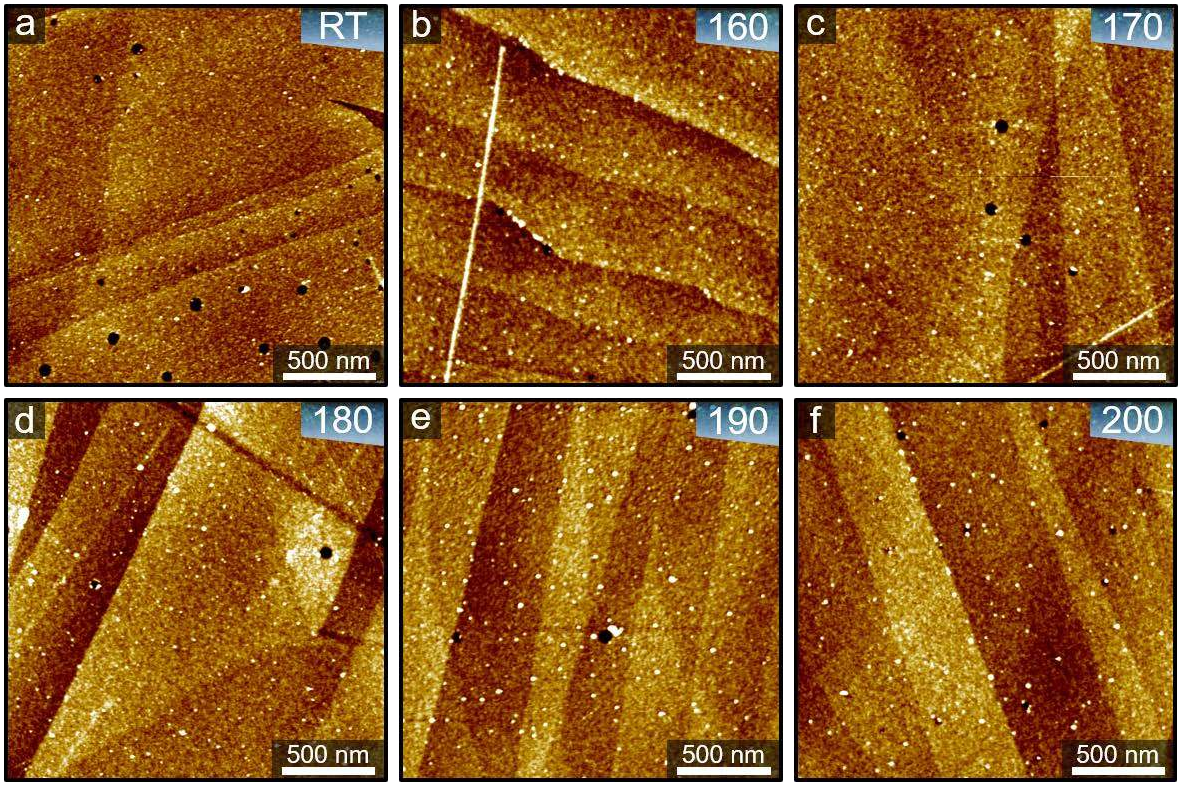

Figure S5. AFM topography images of a 4-NBD modified HOPG substrate at (a) room temperature, and after all stages of the stepwise heating process (b) 160 °C, (c) 170 °C, (d) 180 °C, (e) 190 °C and (f) 200 °C.

S6. Roughness analysis

3,5-TBD	R_a (nm)	R_q (nm)
RT	0.09 ± 0.01	0.12 ± 0.02
160 °C	0.20 ± 0.02	0.25 ± 0.02
170 °C	0.10 ± 0.04	0.15 ± 0.04
180 °C	0.04 ±0.02	0.06 ± 0.03
190 °C	1.2 ± 0.8	1.2 ± 0.7
200 °C	0.6 ± 0.3	0.9 ± 0.2
3,4,5-TMeD	R_a (nm)	R_q (nm)
RT	0.10 ± 0.01	0.13 ± 0.02
160 °C	0.15 ± 0.02	0.21 ± 0.04
170 °C	0.14 ± 0.02	0.19 ± 0.03
180 °C	0.16 ± 0.03	0.21 ± 0.04
190 °C	0.119 ± 0.002	0.154 ± 0.004
200 °C	0.099 ± 0.008	0.13 ± 0.01
3,4,5-TMeOD	R_a (nm)	R_q (nm)
RT	0.21 ± 0.01	0.27 ± 0.02
160 °C	0.25 ± 0.09	0.3 ± 0.1
170 °C	0.26 ± 0.09	0.3 ± 0.1
180 °C	0.27 ± 0.04	0.35 ± 0.05
190 °C	0.37 ± 0.08	0.47 ± 0.09
200 °C	0.26 ± 0.02	0.35 ± 0.03
4-NBD	R_a (nm)	R_q (nm)
RT	0.18 ± 0.02	0.28 ± 0.07
160 °C	0.159 ± 0.005	0.206 ± 0.007
170 °C	0.167 ± 0.008	0.25 ± 0.02
180 °C	0.181 ± 0.004	0.29 ± 0.04
190 °C	0.19 ± 0.02	0.27 ± 0.02
200 °C	0.181 ± 0.005	0.29 ± 0.03

Table S1. Summary of the AFM roughness analysis for all substrate modifications (4-NBD; 3,5-TBD; 3,4,5-TMeD; 3,4,5-TMeOD) at room temperature and all stages of the stepwise heating process. These parameters where collected at three different locations for each data point, by analyzing three 501 × 501 nm^2 zooms with no present graphite step edges. R_a representing the roughness average and R_q the Root Mean Square.

S7. STM data of stepwise heating for 3,5-TBD-G

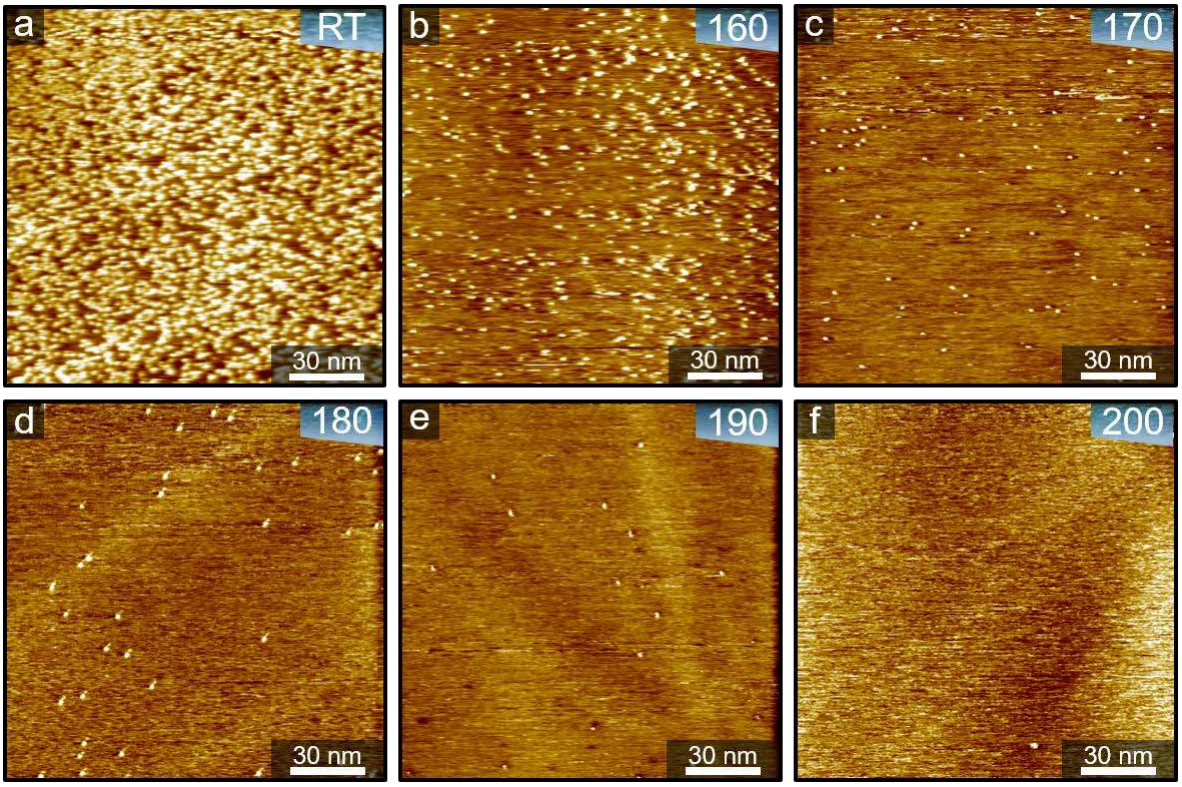

Figure S6. STM current images of a 3,5-TBD modified HOPG substrate at (a) room temperature, and after all stages of the stepwise heating process (b) 160 °C, (c) 170 °C, (d) 180 °C, (e) 190 °C and (f) 200 °C. These images where obtained at following imaging parameters: V_b = –0.8 V, I_t = 50 pA.

S8. STM data of stepwise heating for 3,4,5-TMeD-G

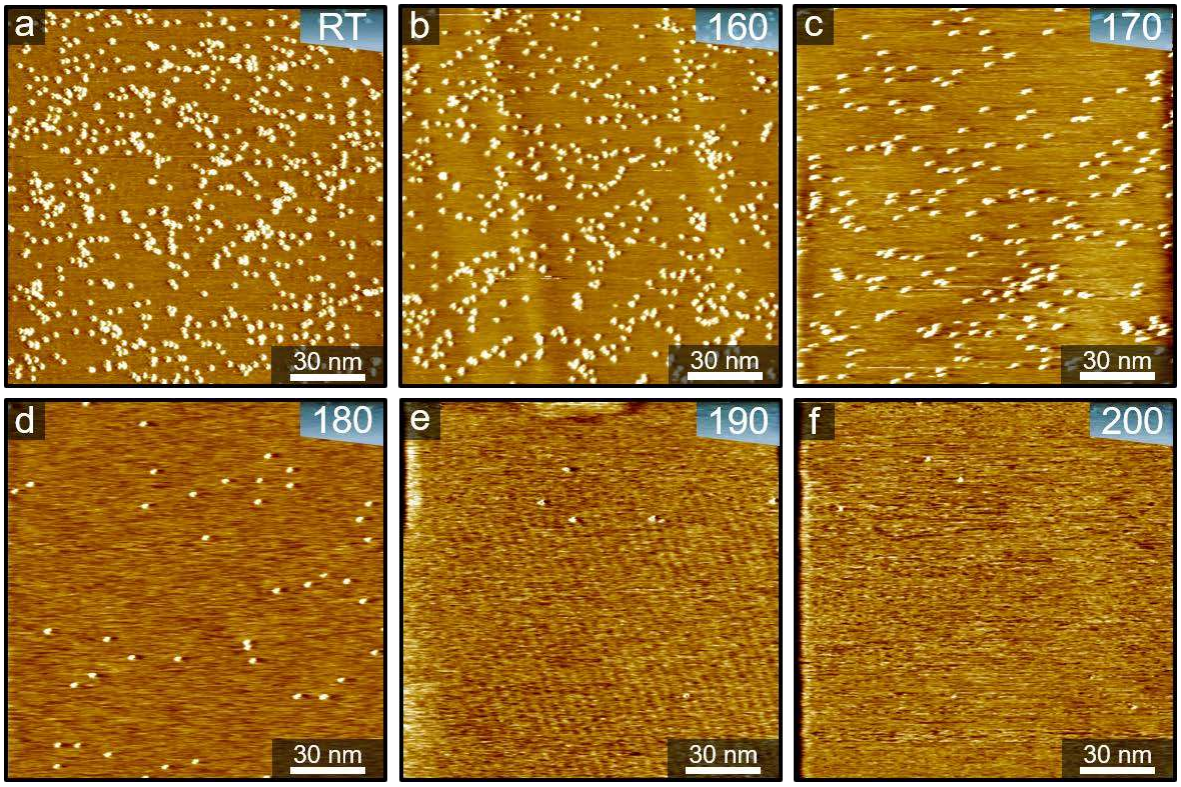

Figure S7. STM current images of a 3,4,5-TMeD modified HOPG substrate at (a) room temperature, and after all stages of the stepwise heating process (b) 160 °C, (c) 170 °C, (d) 180 °C, (e) 190 °C and (f) 200 °C. These images where obtained at following imaging parameters: $V_b = –0.8$ V, $I_t = 50$ pA. The wavy features in some of the STM images are tentatively attributed to self-assembled alkane-type contaminants.

S9. STM data of stepwise heating for 3,4,5-TMeOD-G

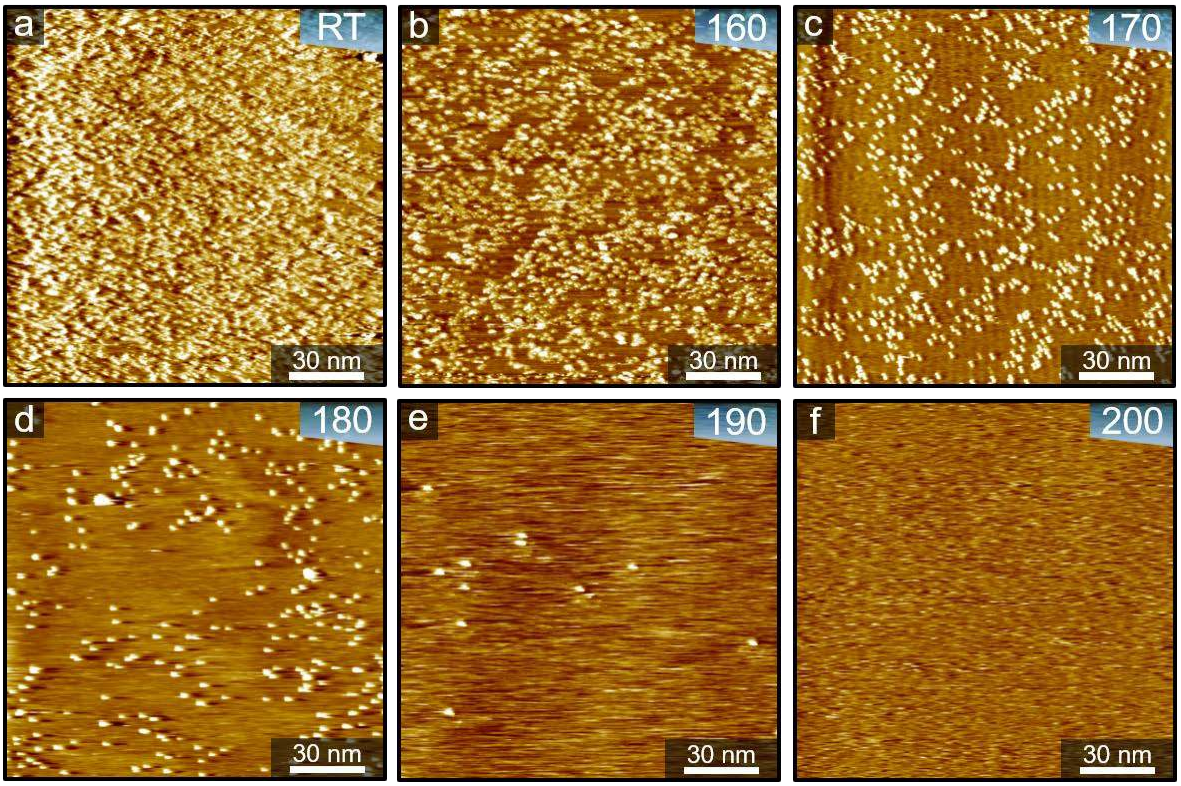

Figure S8. STM current images of a 3,4,5-TMeOD modified HOPG substrate at (a) room temperature, and after all stages of the stepwise heating process (b) 160 °C, (c) 170 °C, (d) 180 °C, (e) 190 °C and (f) 200 °C. These images where obtained at following imaging parameters: V_b = –0.8 V, I_t = 50 pA.

S10. STM data of stepwise heating for 4-NBD-G

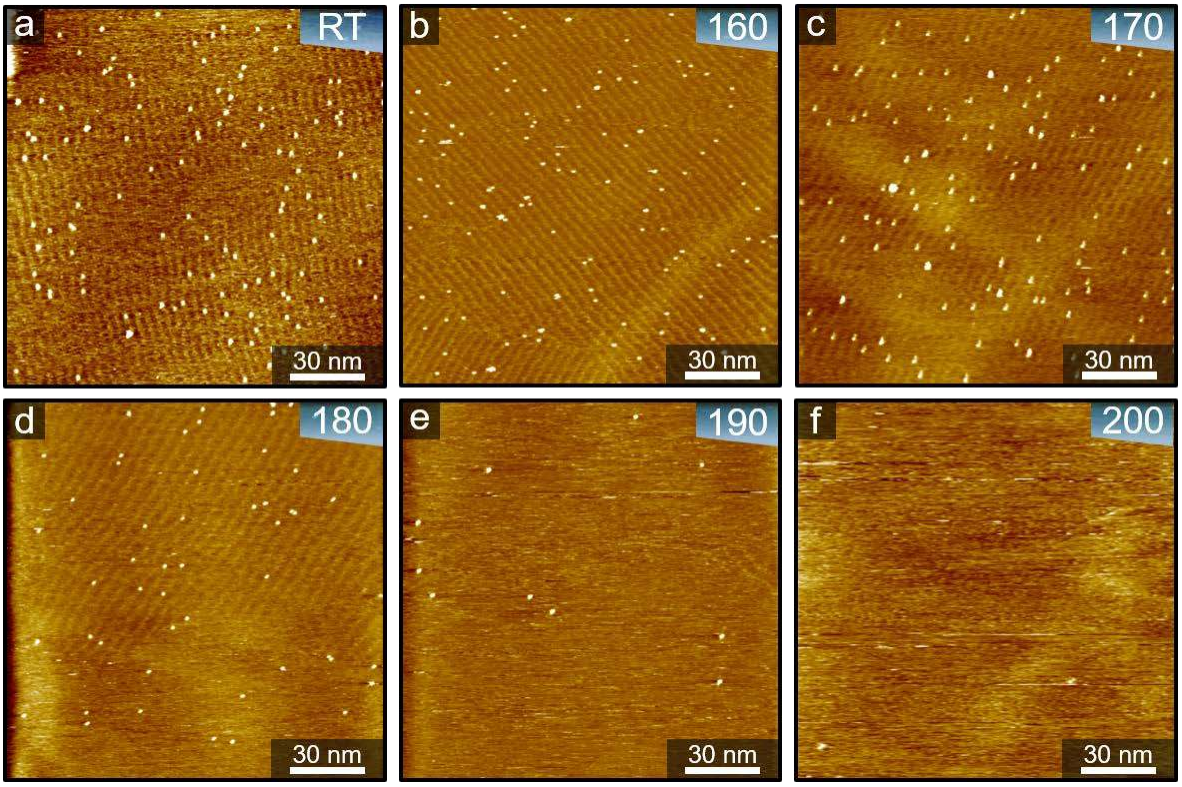

Figure S9. STM current images of a 4-NBD modified HOPG substrate at (a) room temperature, and after all stages of the stepwise heating process (b) 160 °C, (c) 170 °C, (d) 180 °C, (e) 190 °C and (f) 200 °C. These images where obtained at following imaging parameters: V_b = –0.8 V, I_t = 50 pA. The wavy features in some of the STM images are tentatively attributed to self-assembled alkane-type contaminants.

S11. Full Kinetic data from Raman measurements

3,4,5-TMeD		3,4,5-TMeOD		3,5-TBD	
Temp / °C	K / s-1	Temp / °C	K / s-1	Temp / °C	K / s-1
		210	0.020 ± 0.001	160	0.039 ± 0.011
200	0.022 ± 0.006	200	0.010 ± 0.001	150	0.013 ± 0.005
190	0.008 ± 0.002	190	0.0082 ± 0.0007	140	0.0012 ± 0.0001
180	0.0053 ± 0.0008	180	0.0030 ± 0.0006	130	0.0006 ± 0.0001
170	0.0032 ± 0.0005	170	0.0023 ± 0.0003		
160	0.0023 ± 0.0002	160	0.0019 ± 0.0002		

Table S2: summary of the rate constant data for each molecule along with an associated uncertainty (determined as the range divided by 2 times the square root of the number of measurements due to small sample sizes).

S12. Analysis of pre-exponential factors

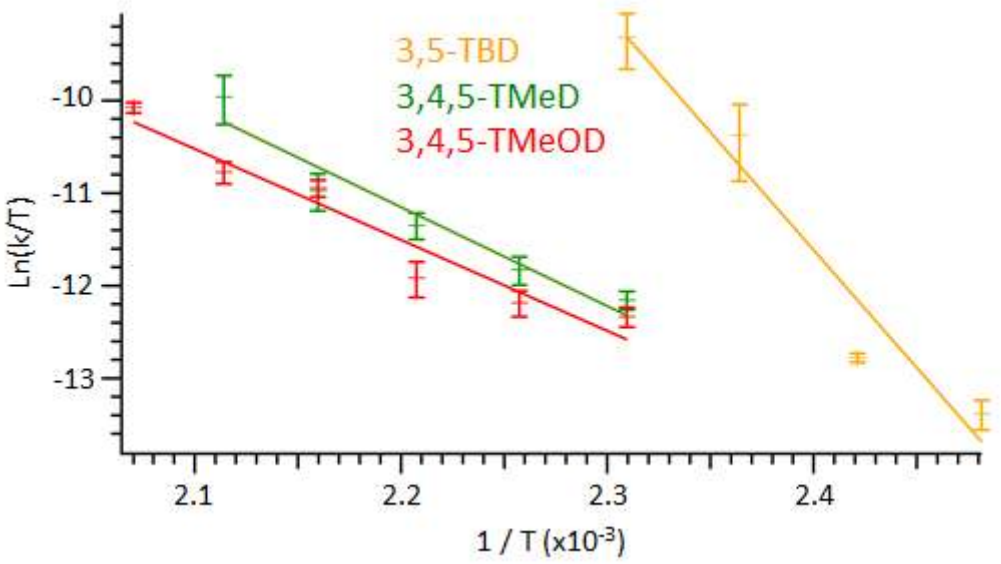

Figure S10: Graph showing ln(k/T) against 1/T used to determine $\Delta S^{\ddagger}$ and $\Delta H^{\ddagger}$ using the Eyring approach, along with linear fits to the data.

S13. Data variability

It was generally observed that the kinetic data for 3,5-TBD-G exhibited a far greater degree of variability than either of the two other molecules included in the study. This is illustrated by in the selection of graphs of normalized raw data given below. Whereas the curves for 3,4,5-TMeD-G and 3,4,5-TMeOD-G appear relatively self-consistent across different measurement sessions (identified by both separate measurement and sample fabrication periods), this is not found to be the case for 3,5-TBD-G. Such variations may be related to the heterogeneous desorption detailed in figure 3/S2.

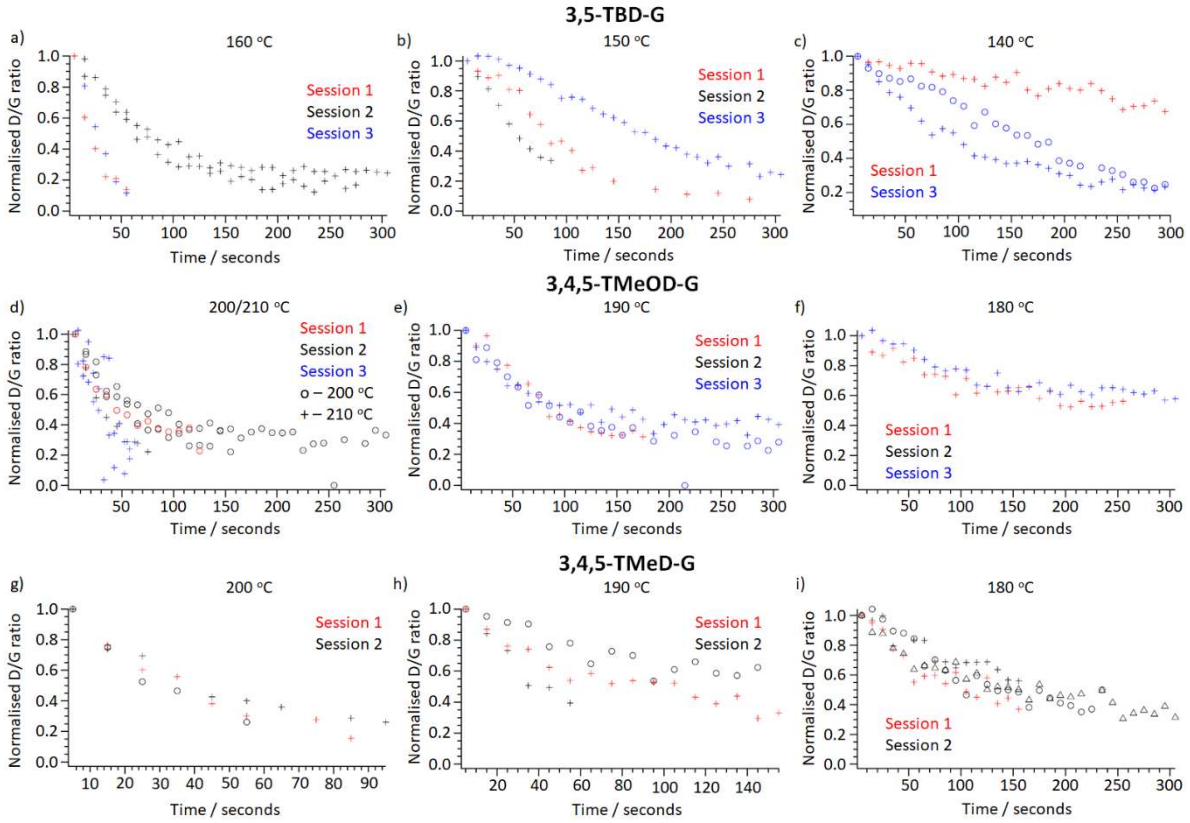

Figure S11: Selection of graphs of normalized (D/G) against time showing reproducibility of measurements across different measurement sessions for 3,5-TBD (a-c), 3,4,5-TMeOD (d-f), and 3,4,5-TMeD (g-i) grafted surfaces.

S14. Second-order fitting

It was considered that the discrepancies found with 3,5-TBD-G may originate from 2nd order behavior. To test for this, figure S12a shows a series of data for 3,5-TBD-G modelled to 2nd order reaction kinetics. Here, the inverse of the normalized (D/G) (i.e. 1/(D/G)) was plotted against time. Figure S12 shows a comparison of fits for a selection of data for 3,5-TBD-G for both a 2nd order (a) and 1st order fit. However, the 2nd order fittings do not appear to yield better results. Indeed, given that in general $ln(\mathrm{D/G})$ yielded a reasonable fit and the temperature range was limited, it was taken in light of this that the use of a 1st order model was a safe assumption.

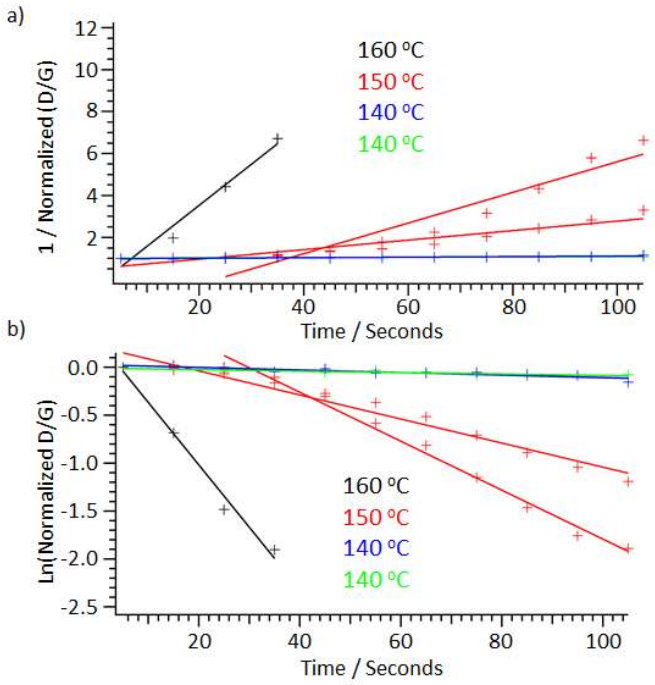

Figure S12: Comparison of 2nd (a) and 1st (b) order fittings to a subsection of kinetic data for 3,5-TBD-G.

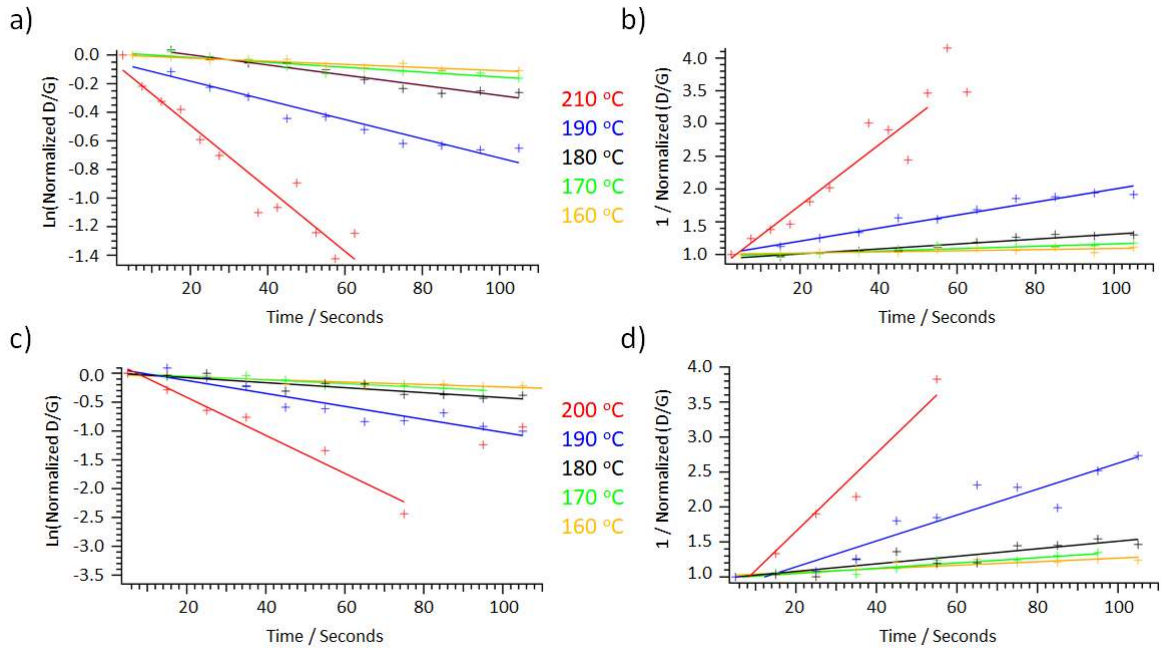

Figure S13: Comparison of and 1st (a, c) and 2nd (b, d) order fittings to a subsection of kinetic data for 3,4,5-TMeOD-G and 3,4,5-TMeD-G, respectively

Considering the results of the Eyring equation, a second order model was also considered for the other two systems studied. Figure S13 compares first and second order models for a subset of the data for 3,4,5-TMeOD-G (a, b) and 3,4,5-TMeD (c, d), respectively. It was indeed possible to fit this data to second order, but this didn't appear to yield an improvement to the individual fittings. Again, given the limited temperature range studied it was thus decided to assume a first order kinetic model. For clarity, figure S14 shows Arrhenius plots for both systems using the rate constants extracted from the second order model. In this case the activation energies were 120 ± 10 kJ mol^{-1} and 100 ± 10 kJ mol^{-1} for 3,4,5-TMeD and 3,4,5-TMeOD, respectively. The corresponding pre-exponential factors were 3×10^{11} (10^{13} – 10^{9}) and 5×10^{9} (10^{8} – 10^{10}).

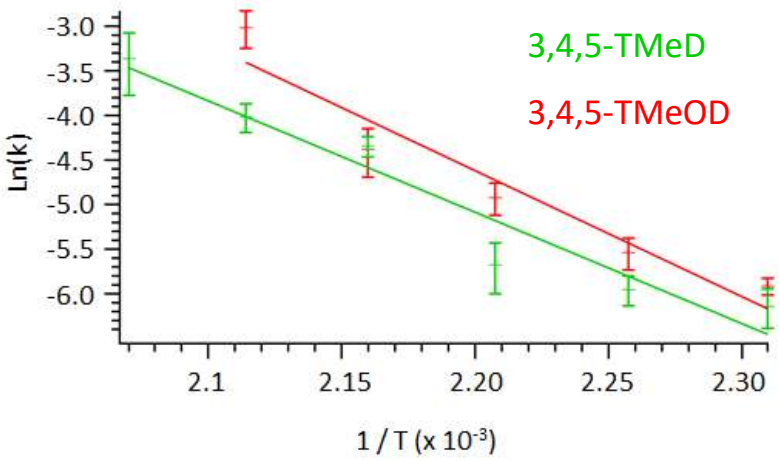

Figure S14: Arrhenius plots for 3,4,5-TMeOD-G and 3,4,5-TMeD-G based on a second order kinetic analysis.